HHS Public Access

Author manuscript

Dev Cell. Author manuscript; available in PMC 2024 June 19.

Published in final edited form as:

Dev Cell. 2023 June 19; 58(12): 1052–1070.e10. doi:10.1016/j.devcel.2023.04.005.

Polycomb Ezh1 maintains murine muscle stem cell quiescence through non-canonical regulation of Notch signaling

Xuesong Feng[1,8], **A. Hongjun Wang**[1,8], **Aster H. Juan**[1,8], **Kyung Dae Ko**[1], **Kan Jiang**[2], **Giulia Riparini**[1], **Veronica Ciuffoli**[1], **Aissah Kaba**[1], **Christopher Lopez**[1], **Faiza Naz**[3], **Michal Jarnik**[4], **Elizabeth Aliberti**[1], **Shenyuan Hu**[5], **Jessica Segalés**[6], **Mamduh Khateb**[1], **Natalia Acevedo-Luna**[1], **Davide Randazzo**[7], **Tom H. Cheung**[5], **Pura Muñoz-Cánoves**[6], **Stefania Dell'Orso**[3], **Vittorio Sartorelli**[1,*]

[1]Laboratory of Muscle Stem Cells & Gene Regulation, NIAMS, NIH, Bethesda, USA

[2]Biodata Mining & Discovery Section, NIAMS, NIH, Bethesda, USA

[3]Genomic Technology Section, NIAMS, NIH, Bethesda, USA

[4]Cell Biology and Neurobiology Branch, NICHD, NIH, Bethesda, USA

[5]Division of Life Sciences, State Key Laboratory of Molecular Neuroscience Center, The Hong Kong University of Science and Technology, Hong Kong, China

[6]Department of Experimental and Health Sciences, UPF, ICREA, CIBERNED, Barcelona, Spain

[7]Light Imaging Section, NIAMS, NIH, Bethesda, USA

[8]These authors contributed equally

Summary

Organismal homeostasis and regeneration are predicated on committed stem cells which can reside for long periods in a mitotically dormant but reversible cell cycle arrest state defined as quiescence. Premature escape from quiescence is detrimental as it results in stem cell depletion, with consequent defective tissue homeostasis and regeneration. Here, we report that Polycomb Ezh1 confers quiescence to murine muscle stem cells (MuSCs) through a non-canonical function. In the absence of Ezh1, MuSCs spontaneously exit quiescence. Following repeated injuries, the

*Lead contact and correspondence: Vittorio.Sartorelli@nih.gov.

AUTHOR CONTRIBUTIONS

X.F., A.HJ.W., A.H.J., S.D.O., and V.S. conceived the project, designed the experiments, performed experiments, and interpreted data. X.F., A.HJ.W., A.H.J., S.D.O. performed ChIP-qPCR, RNA-seq, ATAC-seq, and scATAC-seq experiments. X.F. supervised animal crossing, performed histology, immunostaining, and confocal microscopy experiments. F.N. performed immunostaining. A.HJ.W. performed transfections, luciferase assay, and immunoblotting experiments. K.D.K. and K.J. analyzed RNA-seq, scRNA-seq, and ATAC-seq experiments. G.R., A.K., C.L., E.A., V.C., S.H., J.S. isolated MuSCs by FACS, prepared primary myoblasts, performed immunoblotting, and analyzed MuSCs. M.J. performed electron microscopy. N.A-L provided bioinformatic advice. M.K. provided biochemical advice. D.R. provided assistance with microscopy. T.C. supervised S.H., P.M-C. supervised J.S. V.S. supervised research and wrote the manuscript with input from all co-authors.

DECLARATION OF INTERESTS

The authors declare no competing interests.

MuSC pool is progressively depleted resulting in failure to sustain proper muscle regeneration. Rather than regulating repressive histone H3K27 methylation, Ezh1 maintains gene expression of the Notch signaling pathway in MuSCs. Selective genetic reconstitution of the Notch signaling corrects stem cell number and re-establishes quiescence of *Ezh1*$^{-/-}$ MuSCs.

Graphical Abstract

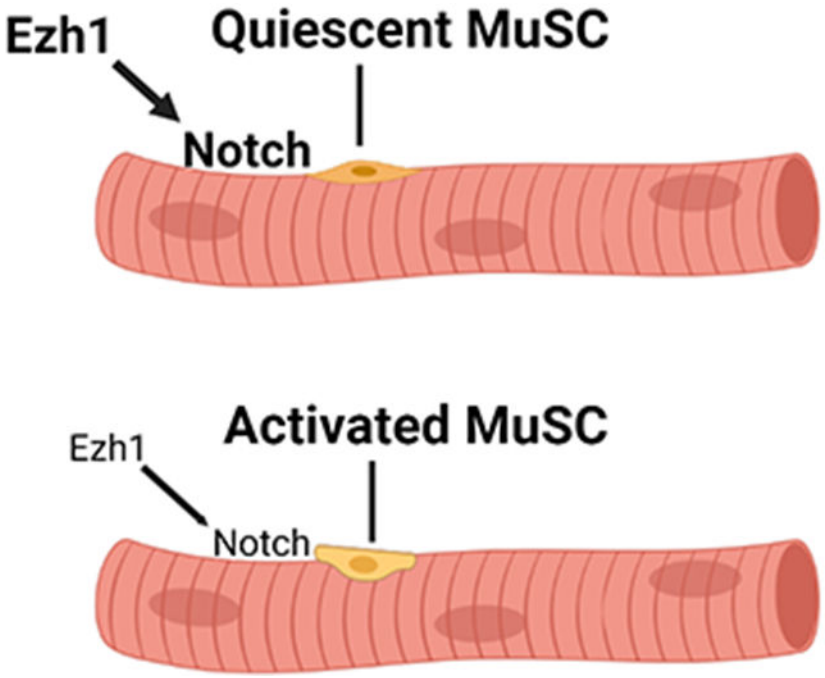

eTOC

Feng et al. report that Ezh1 maintains murine muscle stem cell quiescence by regulating expression of the Notch signaling pathway.

Introduction

Adult somatic stem cells (ASCs) replace lost tissue through cell division, thereby ensuring tissue homeostasis [1]. Muscle resident ASCs (satellite cells or Muscle Stem Cells, MuSCs) confer homeostatic and regenerative properties to skeletal muscle [2-7]. Otherwise quiescent, MuSCs become alerted or activated in response to wounding or exercise and undergo cell division, giving rise to either daughter progeny that returns to quiescence or muscle progenitors which, after expansion, differentiate and fuse into new or preexisting muscle fibers [8-13]. In a remarkable experiment, transplantation of a single MuSC was shown to generate tens of thousands of cells contributing to muscle fibers [14]. Inability to ensure an appropriate balance between quiescence and activation results in defective regulation of several ASCs, including neuronal [15], hematopoietic [16], and MuSCs [17-19].

Return to quiescence requires that chromatin domains be re-established after mitosis [20]. This process entails correct repositioning of repressive histone post-translational modifications

that are epigenetically inherited to prevent inappropriate gene activation [21]. The Polycomb repressive complex 2 (PRC2), composed of core subunits Ezh2/Ezh1, Suz12, and Eed, initiates deposition and maintenance of the repressive H3K27me3 histone mark [22-26]. Ezh2 safeguards MuSCs transcriptional identity and proliferation [27,28], regulates proliferation of epidermal progenitors [29], B and T cell development [30 31], specification and differentiation of cerebellar and cortical neurons [32 33]. Ezh2 and other PRC2 subunits also control the fates of human and mouse embryonic stem cells [34-37], intestinal progenitors [38], hematopoietic stem cells [39], germ cells [40], and additional cell types [41]. Consistent with its role in re-establishing H3K27me3 chromatin domain after mitosis, Ezh2 is expressed in proliferating cells and is undetectable in quiescent MuSCs [27,42]. Instead, Ezh1 is preferentially expressed in non-proliferative cells [43], suggesting distinct functions of the two paralogs. The cellular context and genetic program determine whether Ezh1 represses or activates gene expression [43-53]

Here, we report a role for Polycomb group Ezh1 in MuSCs biology. In contrast to its paralog Ezh2, which is required for expansion of muscle progenitors [27,28], Ezh1 maintains MuSCs quiescence. In the absence of Ezh1, MuSCs are spontaneously activated but then fail to sustain proper regeneration. This phenomenon is associated with impaired quiescence and increased propensity of *Ezh1*$^{-/-}$ MuSCs to differentiate. Defective return to quiescence is cell-autonomous as transplanted *Ezh1*$^{-/-}$ MuSCs do not efficiently re-occupy their niche after injury. Mechanistically, Ezh1 controls the Notch pathway and ciliogenesis, which are both impaired in *Ezh1*$^{-/-}$ MuSCs. In keeping with these findings, selective genetic reconstitution of the Notch signaling in MuSCs corrects MuSCs number and ciliogenesis, and re-establishes *Ezh1*$^{-/-}$ MuSCs quiescence.

RESULTS

Ezh1 is enriched in freshly isolated MuSCs

Comparison of RNA-seq from freshly FACS-isolated and 48hr-activated MuSCs [54] revealed enrichment of Ezh1, Pax7, Spry1 and Notch3 transcripts in freshly isolated MuSCs and of Ezh2, MyoD, the glycolytic enzyme Pkm, and the initiation factor Eif4a1 in activated MuSCs (Supplemental Figure S1A,B). We evaluated *in vivo* Ezh1 and Ezh2 expression during muscle regeneration in single cell RNA-seq (scRNA-seq) datasets obtained from MuSCs isolated from *tibialis anterior* (TA) muscles of uninjured or 60hr-post injured mice [55]. Ezh1 expression was highest in MuSCs of unperturbed muscles (0hr), progressively declining in 60hr-post injury MuSCs. In contrast, Ezh2 transcripts, lowly expressed in MuSCs of unperturbed muscles, gradually increased in MuSCs derived from injured muscles, coinciding with increased expression of Myogenin (Supplemental Figure S1C). Mining published datasets [56], we evaluated expression of Ezh1 and other PRC2 and PRC1 subunits in aged MuSCs. Aged MuSCs lose their ability to retain quiescence and are primed for differentiation [57 58]. Consistent with increased H3K27me3 levels [59], aged MuSCs display increased expression of Ezh2 and Eed. Instead, Ezh1 and Suz12 are reduced in aged MuSCs. PRC1 subunits Bmi1 and Pcgf1 are also differentially expressed in young and aged MuSCs (Supplemental Figure S1D). Thus, the two Polycomb paralogs Ezh1 and Ezh2 display mirrored expression patterns, with Ezh1 prevailing in freshly isolated young MuSCs and Ezh2 in activated or aged MuSCs.

Ezh1 regulates the transcriptome of MuSCs

To investigate the impact of Ezh1 on gene transcription, we FACS-purified MuSCs from the hindlimbs of littermate wild-type (WT) or *Ezh1*$^{-/-}$ mice (Supplemental Figure S1E,F) and profiled their transcriptomes by RNA-seq. Transcripts corresponding to 365 and 418 genes were either up- or down-regulated in *Ezh1*$^{-/-}$ MuSCs (Supplemental Table S1). Transcripts enriched in *Ezh1*$^{-/-}$ MuSCs are related to RNA metabolism, ribonucleoprotein complex biogenesis, receptor tyrosine kinase signaling (RTK), and the ERK1/ERK2 cascade (Figure 1A,C). RNA biogenesis is rapidly initiated at the earliest steps of MuSC activation [55,60,61], and ERK1/ERK2 and RTK signaling promote MuSC activation and cell cycle entry [62-64]. Transcripts corresponding to muscle proteins troponins (Tnnc2, Tnnt3), actin (Acta1), myosin (Mylpf), and muscle creatine kinase (Ckm) were enriched in *Ezh1*$^{-/-}$ MuSCs (Figure 1C and Supplemental Table S1). Of the 365 transcripts up-regulated in *Ezh1*$^{-/-}$ MuSCs, only 7 were up-regulated in *Ezh2*$^{-/-}$ MuSCs [28] (Supplemental Table S1), indicating distinct functions of the two Ezh paralogs. Expression of the Polycomb target cyclin-dependent kinase inhibitor Cdkn2a (p16-INK4A-ARF), which is increased in *Ezh2*$^{-/-}$ MuSCs [27 28], was unmodified in *Ezh1*$^{-/-}$ MuSCs (Supplemental Table S1).

Genes whose expression was reduced in *Ezh1*$^{-/-}$ MuSCs regulate unfolded protein response (UPR), DNA damage response, cell cycle, and regulation of cellular responses to stress (Figure 1B,C and Supplemental Table S1). Transcripts of numerous heat shock proteins (HSPs), which are highly enriched in freshly isolated MuSCs [65], were decreased in *Ezh1*$^{-/-}$ MuSCs (Supplemental Table S1). HSPs maintain stem cell proteostasis by acting as chaperones [66,67]. Expression of DNA repair and response to stress genes was also diminished in *Ezh1*$^{-/-}$ MuSCs (Supplemental Table S1). MuSCs repair DNA double-strand breaks more efficiently than their committed progeny and are relatively resistant to apoptosis [68]. Transcripts for effectors and targets of the Notch pathway, required to maintain MuSC quiescence, basal lamina assembly, and adhesion [69 70 71 72], were reduced in *Ezh1*$^{-/-}$ MuSCs (Figure 1C and Supplemental Table S1). More specifically, Rbpj, Notch1, Notch3, and the Notch targets Hey1, Hes1, Chd15, and Serinc5 [73] were decreased in *Ezh1*$^{-/-}$ MuSCs (Figure 1C and Supplemental Table S1). We wished to evaluate to which temporal activation state the *Ezh1*$^{-/-}$ MuSCs transcriptome most closely resembles. To this end, we compared transcripts enriched or depleted in *Ezh1*$^{-/-}$ MuSCs with those of MuSCs immediately fixed in situ, freshly isolated and fixed after 3 (T3-T0, early activation) or 5 (T5-T0, later activation) hours [60] (Supplemental Table S2). This analysis revealed that 44% of up-regulated and 56% of down-regulated transcripts in *Ezh1*$^{-/-}$ MuSCs were also increased and decreased in early activated (T3-T0) MuSCs, respectively. The percentage of shared transcripts decreased to 31% for up-regulated and to 50% for down-regulated genes in later activated T5-T0 MuSCs. Focusing on transcripts modulated in a 2 hr interval (T5-T3), *Ezh1*$^{-/-}$ and T5-T3 MuSCs shared only 0.08% up-regulated and one down-regulated transcript (0.002%) (Supplemental Table S2). Overall, this analysis indicates that a substantial amount of transcriptional changes occurring in *Ezh1*$^{-/-}$ MuSCs are also observed in early activated MuSCs (T3-T0) and are lost when MuSCs are activated for additional time (T5-T3). Ezh1, Notch3, Hes1, Hey1, and Chd15 transcripts were also reduced in early activated T3-T0 MuSCs compared to fixed (quiescent) MuSCs [60]. To gauge single-cell level transcription and MuSCs heterogeneity, we FACS-isolated MuSCs from WT or *Ezh1*$^{-/-}$

mice and performed scRNA-seq. Unsupervised clustering of WT and *Ezh1*$^{-/-}$ MuSCs returned three adjacent yet distinct cell clusters: i) shared by WT and *Ezh1*$^{-/-}$ MuSCs (WT+*Ezh1*$^{-/-}$); ii) specific to WT MuSCs; and iii) specific to *Ezh1*$^{-/-}$ MuSCs (*Ezh1*$^{-/-}$) (Figure 1D, top panel). Transcript analyses identified the top differentially expressed genes between the WT and *Ezh1*$^{-/-}$ clusters (Figure 1E). Transcripts that were decreased in the *Ezh1*$^{-/-}$ cluster included: Pax7, a transcription factor expressed in MuSCs [74] and activated by Notch signaling [75] (Figure 1F); Spry, an RTK inhibitor required to return to quiescence of self-renewing MuSCs [76] (Figure 1F); and Meg3, a long noncoding RNA expressed in freshly isolated MuSCs [65 58], and regulating muscle development [77] (Figure 1F). On the other hand, transcripts that were enriched in the *Ezh1*$^{-/-}$ cluster included ribosomal 60S protein transcripts Rpl29 and Rpl38 and 40S Rsp25, which are up-regulated in activated MuSCs [54] (Figure 1F). Single-cell expression datasets were pseudotemporally ordered to monitor the transitions between different MuSC developmental states. This analysis revealed that cells hosted in the shared WT+*Ezh1*$^{-/-}$ cluster retained the most undifferentiated transcriptome. Instead, the *Ezh1*$^{-/-}$ cluster hosted MuSCs with transcriptomes with the farthest progression towards differentiation compared to other clusters (yellow, Figure 1D, bottom panel). This analysis revealed that cells with shared WT and *Ezh1*$^{-/-}$ transcriptomes display very subtle transcriptional differences. Overall, these data indicate that Ezh1 controls expression of genes involved in several important pathways that regulate MuSCs biology and suggest its role in maintaining transcriptional MuSC quiescence.

Ezh1 confers quiescence by restraining MuSCs activation and differentiation

When quiescent MuSCs are activated, they increase their cell size and RNA content, accumulate MyoD protein, and are prone to enter the S-phase of cell cycle [55,78-80]. We therefore compared these parameters between WT and *Ezh1*$^{-/-}$ MuSCs and found that *Ezh1*$^{-/-}$ MuSCs had increased cell size and RNA content (Figure 2A,B and Supplemental Figure S2A). Using time-lapse microscopy, we observed that MuSCs isolated from *Ezh1*$^{-/-}$ mice completed their first cell division before those isolated from WT mice (Figure 2C and Supplemental Figure S2B). A higher percentage of myofiber-associated *Ezh1*$^{-/-}$ MuSCs incorporated the thymidine analog EdU, indicating that they had entered S-phase, as compared to WT MuSCs (Figure 2D). Activated MuSCs express both Pax7 and MyoD proteins, while quiescent MuSCs accumulate only Pax7 protein [79]. Immunofluorescence staining revealed a lower percentage of MyoD^{-}/Pax7^{+} MuSCs, and a higher percentage of MyoD^{+}/Pax7^{+} MuSCs in *Ezh1*$^{-/-}$ myofibers (Figure 2E). In addition, we isolated primary myoblasts from WT or *Ezh1*$^{-/-}$ mice, cultured them in conditions favoring growth and antagonizing differentiation, and analyzed their transcriptomes by scRNA-seq. We found that Myogenin, a marker of cell differentiation, was expressed in 18% of WT myoblasts and in 42% of *Ezh1*$^{-/-}$ myoblasts (Figure 2F). Together, these data indicate that *Ezh1*$^{-/-}$ myoblasts are more likely to differentiate.

MuSCs contribute to myonuclear accretion in homeostatic conditions [3 4]. We wished to ascertain whether MuSCs might spontaneously enter S-phase in uninjured mice and, for this, we lineage-traced MuSCs by crossing tamoxifen-inducible *Pax7*^{CreERT2} [81] with *ROSA26*$^{STOP\text{-}Sun1\text{-}GFP}$ mice [82]. In these mice, individual MuSCs can be identified and quantified by expression of the nuclear membrane-

bound Sun1-GFP fusion protein. Tamoxifen-treated *Pax7*^{CreERT2};*ROSA26*$^{STOP\text{-}sun1\text{-}GFP}$ or Pax7^{CreERT2}; *ROSA26*$^{STOP\text{-}Sun1\text{-}GFP}$; *Ezh1*$^{-/-}$ mice were peritoneally injected with EdU for 14 consecutive days, after which hindlimb muscle sections were obtained and processed for GFP and EdU staining. The percentage of GFP^+/EdU^+ double-positive cells doubled in Pax7^{CreERT2}; *ROSA26*$^{STOP\text{-}Sun1\text{-}GFP}$; *Ezh1*$^{-/-}$ compared to *Pax7*^{CreERT2};*ROSA26*$^{STOP\text{-}Sun1\text{-}GFP}$ WT muscle (Figure 2G), indicating increased *in vivo* spontaneous activation of *Ezh1*$^{-/-}$ MuSCs. Overall, these findings indicate that *Ezh1*$^{-/-}$ MuSCs prematurely exit quiescence and undergo early activation.

Ezh1 does not influence histone H3K27me3 in MuSCs

Ezh1 promotes H3K27methylation [43,83]. To assess whether Ezh1 contributes to H3K27me3 in quiescent MuSCs *in vivo*, muscle cross-sections were obtained from littermate WT or *Ezh1*$^{-/-}$ mice and MuSCs identified by Pax7 and H3K27me3 co-immunostaining. No obvious difference in MuSC H3K27me3 staining intensity was noted (Supplemental Figure S3A). Similarly, immunoblotting of cell extracts derived from WT or *Ezh1*$^{-/-}$ MuSCs revealed no apparent differences in H3K27me3 levels (Supplemental Figure S3B). Ezh2 is not detectable in quiescent MuSCs [27 42] and we did not detect increase of Ezh2, Suz12, or Eed transcripts in *Ezh1*$^{-/-}$ MuSCs, compared to WT MuSCs (Supplemental Figure S3C and Supplemental Table S1), ruling out a compensatory role of other PRC2 subunits in maintaining H3K27me3 levels in *Ezh1*$^{-/-}$ MuSCs. Since immunofluorescence and immunoblotting assays do not distinguish chromatin-bound from soluble histones, we evaluated chromatin-associated H3K27me3 histones by ChIP-seq (Supplemental Figure S3 and Supplemental Table S3). Non significant changes in either genome-wide distribution or enrichment of H3K27me3 were observed with comparable percentage of H3K27me3 peaks occurring at TSS (which were selected to identify their cognate genes), intergenic, or other genomic regions of WT and *Ezh1*$^{-/-}$ MuSCs. The nucleotide composition of H3K27me3-occupied regions was also comparable in WT and *Ezh1*$^{-/-}$ MuSCs (Supplemental Figure S3D,E). H3K27me3 signal at Polycomb-target homeotic (*Hox*) genes was similar and *Ckm* and *Tnnt3* genes retained comparable H3K27me3 in WT and *Ezh1*$^{-/-}$ MuSCs (Supplemental Figure S3F). Overall, these results indicate that Ezh1 deletion does not affect H3K27me3 in MuSCs.

Ezh1 controls chromatin accessibility and compaction

Ezh1 favors chromatin compaction independently of its methyltransferase activity [43]. Probing the chromatin state by ATAC-seq revealed that *Ezh1*$^{-/-}$ MuSCs had increased chromatin accessibility, compared to WT MuSCs (Figure 3A,B). Quiescent MuSCs are characterized by highly dense and compacted heterochromatin that can be visualized by transmission electron microscopy (TEM) [42,84]. To evaluate whether increased chromatin accessibility in *Ezh1*$^{-/-}$ MuSCs was accompanied by visibly reduced chromatin compaction, we prepared ultra-thin muscle sections of WT or *Ezh1*$^{-/-}$ mice and analyzed them by TEM. *Ezh1*$^{-/-}$ muscle sections hosted MuSCS with reduced condensed heterochromatin compared to WT sections (Figure 3C). As increased chromatin accessibility is often associated with increased gene expression, we correlated ATAC-seq and RNA-seq datasets from WT and *Ezh1*$^{-/-}$ MuSCs. Increased chromatin accessibility in *Ezh1*$^{-/-}$ MuSCs occurred at promoter regions of genes with increased gene expression (Figure 3D, red dots). Genes up-regulated

in *Ezh1*$^{-/-}$ and in activated MuSCs displayed increased chromatin accessibility in both *Ezh1*$^{-/-}$ MuSCs and activated MuSCs [85] (Supplemental Table S2). Surprisingly, genes with decreased expression were also more accessible in *Ezh1*$^{-/-}$ MuSCs (Figure 3D, blue dots). Thus, while confirming observations obtained in other experimental systems that Ezh1 regulates chromatin accessibility and compaction [43 86], our findings indicate that in MuSCs chromatin changes caused by Ezh1 deletion do not unequivocally correlate with gene expression and may be more related to higher-order structure than function.

Muscle regeneration is impaired in the absence of Ezh1

Mice lacking *Ezh1* (https://www.informatics.jax.org/allele/MGI:4941012) are viable, fertile, and healthy [44]. Indeed, the skeletal muscles of *Ezh1*$^{-/-}$ mice were histologically indistinguishable from those of WT mice. Muscle fiber cross-sectional area, number of MuSCs (Pax7^{+}), macrophages (F4/80^{+}), fibro-adipogenic progenitors (FAPs) (Pdgfra^{+}), and collagen deposition were comparable in uninjured WT and *Ezh1*$^{-/-}$ mice (Supplemental Figure S4A-E). We reasoned that assessing potential differences between WT and *Ezh1*$^{-/-}$ mice may require actively engaging MuSCs. To this end, TA muscles of WT or *Ezh1*$^{-/-}$ mice were injured with notexin (NTX) and collected after twenty-eight (28) days. The myofiber cross-sectional area (CSA) of NTX-injected *Ezh1*$^{-/-}$ mice was comparable to that of WT mice (Supplemental Figure S5A). However, the number of Pax7^{+} cells was decreased in NTX-injected *Ezh1*$^{-/-}$ mice (Supplemental Figure S5B). This suggested that *Ezh1*$^{-/-}$ MuSCs may be partially defective in re-establishing the stem cell pool. Thus, we performed an additional NTX injection (28 days post-1st injury) and collected regenerating muscles at either 3 or 28 days post-2nd injury (Figure 4A). MuSCs reach their proliferation zenith three (3) days post injury (dpi), and initiate to differentiate and start reacquiring quiescence approximately seven (7) dpi. Twenty-eight (28) dpi most MuSCs are quiescent [87 88]. At 3 days post-2nd injury, regenerating MuSCs were FACS-isolated and analyzed by scRNA-seq. Unsupervised clustering of MuSCs obtained from either WT or *Ezh1*$^{-/-}$ mice were compared to transcriptomes of FACS-isolated MuSCs and primary myoblasts [55] using a pipeline that correlates single-cell transcriptomes with reference transcriptomic data sets and improves inference iteratively [89]. Differentially-expressed genes in quiescent MuSCs, proliferating myoblasts (PM), and differentiating myocytes (DM) in the reference set [55] were identified and unbiasedly correlated with the transcriptomes of WT or *Ezh1*$^{-/-}$ MuSC scRNA-seq clusters. Clusters of FACS-isolated regenerating MuSCs from WT or *Ezh1*$^{-/-}$ mice shared transcriptomes with proliferating myoblasts of the reference set (Figure 4B, PM, grey). In addition, MuSCs isolated from regenerating *Ezh1*$^{-/-}$ mice formed a subcluster, which was not observed in WT regenerating MuSCs, expressing transcripts present in differentiating myocytes of the reference set (Figure 4B, DM, red). These findings prompted us to investigate MuSC quiescence, activation, and differentiation properties by immunostaining muscle sections with Pax7, MyoD, and Myogenin antibodies. At 3 days post-2nd injury, muscle sections revealed that Pax7^{+} cells were decreased while MyoD^{+} and Myogenin^{+} cells were increased in *Ezh1*$^{-/-}$ mice (Figure 4C-E), indicating activation and premature differentiation of *Ezh1*$^{-/-}$ muscle progenitors. At 28 days post-2nd injury, the number of Pax7^{+} cells was decreased by approximately 40% and the muscle cross-sectional area was significantly reduced in *Ezh1*$^{-/-}$ mice (Figure 4F,G). Centrally located myonuclei and infiltrating macrophages (F4/80^{+}) were not increased (Supplemental Figure S5C-D)

while, consistent with regenerating defects [90], number of FAPS and collagen deposition were increased in *Ezh1*$^{-/-}$ mice (Supplemental Figure S5E-F). Neither Cdkn2a (p16-INK4A-ARF) nor apoptosis was increased in regenerating *Ezh1*$^{-/-}$ MuSCs (Supplemental Figure 5G,H). These findings indicate that, while dispensable for development, Ezh1 is required for muscle regeneration.

Ezh1$^{-/-}$ MuSCs fail to efficiently return to the niche

We sought to determine whether transcriptional dysregulation observed in *Ezh1*$^{-/-}$ MuSCs was translated in cell-autonomous regenerative defects *in vivo*. To trace the fate of MuSCs, we injected *Pax7*^{CreERT2};*ROSA26*$^{STOP\text{-}Sun1\text{-}GFP}$ or *Pax7*^{CreERT2};*ROSA26*$^{STOP\text{-}Sun1\text{-}GFP}$;*Ezh1*$^{-/-}$ mice with tamoxifen to activate GFP expression, FACS-isolated GFP^{+} cells and then immediately transplanted them into NTX pre-injured TA muscles of immunodeficient NRG mice (Figure 5A,B). The transplanted mice were allowed to recover for 28 days, reinjured, and analyzed 28 days post 2nd-injury. This protocol was designed to permit transplanted MuSCs to undergo two rounds of injury/regeneration, a condition under which *Ezh1*$^{-/-}$ mice displayed overt regenerative defects (Figure 4). Muscle sections were obtained and transplanted MuSCs identified by nuclear membrane GFP (nGFP) reactivity. Approximately a month after injury, proliferation ceases and MuSCs either differentiate into new or pre-existing myofibers or return to quiescence, express Pax7, and occupy their niche under the basal lamina [76,87]. To determine grafting efficiency and the percentage of transplanted MuSCs that returned to quiescence, we immunostained muscle sections with a Pax7 antibody and enumerated Pax7^{+}/nGFP^{+} cells. While the overall number of nGFP^{+} cells was comparable, transplanted *Ezh1*$^{-/-}$ MuSCs nGFP^{+} contributed only one-third of Pax7^{+}/nGFP^{+} cells located under the basal lamina, compared to transplanted WT MuSCs. A higher percentage of *Ezh1*$^{-/-}$ Pax7^{-}/nGFP^{+} cells were observed to reside in the myofibers compared to WT Pax7^{-}/nGFP^{+} cells (Figure 5C). No nGFP^{+} cells were observed in the interstitium. These results indicate that, while *Ezh1*$^{-/-}$ MuSCs retain grafting capability, they fail to return to their niche efficiently.

Ezh1 targets the Notch pathway and cilium genes

Expression of members of the Notch pathway is decreased in *Ezh1*$^{-/-}$ MuSCs (Figure 1 and Supplemental Table S1). Hes1, a Notch target, was reduced in regenerating *Ezh1*$^{-/-}$ MuSCs (Figure 6A). We monitored Notch activity in primary myoblasts employing a Notch reporter construct. Transcriptional activity of the Notch reporter was significantly decreased in *Ezh1*$^{-/-}$ myoblasts (Figure 6B). Reduced Notch reporter activity may be directly or indirectly related to the absence of endogenous Ezh1. To differentiate between primary and secondary effects, we reintroduced Ezh1 in *Ezh1*$^{-/-}$ myoblasts and observed that expression of exogenous Ezh1 could restore the Notch reporter activity. Since H3K27me3 was not modified in *Ezh1*$^{-/-}$ MuSCs (Supplemental Figure S3), we also tested whether expression of Ezh1 deleted of the catalytic SET domain (Ezh1$^{\Delta SET}$) could rescue the Notch reporter activity in *Ezh1*$^{-/-}$ myoblasts. Indeed, Ezh1$^{\Delta SET}$ expression was as effective as full length Ezh1 in restoring Notch activity (Figure 6B). To further evaluate whether Ezh1 may directly regulate expression of the Notch pathway in MuSCs, we performed chromatin immunoprecipitation with either control IgG or Ezh1 antibodies followed by quantitative PCR (ChIP-qPCR) at regulatory regions of members of the Notch pathway downregulated in

Ezh1$^{-/-}$ MuSCs. The Ezh1 antibody that we used specifically recognizes Ezh1 and not Ezh2 [47,48]. Ezh1 binding was detected at: i) the Hes1 promoter, in a region occupied by Rbpj [73], ii) the Hey1 promoter [91], and iii) an intronic regulatory region of Notch3 [92] (Figure 6C).

Transcripts involved in cilia formation are highly enriched in quiescent and decline in activated MuSCs [60]. Expression of several cilium genes was decreased in *Ezh1*$^{-/-}$ MuSCs, including Arl13b, IFT88, Bbs7, CEP170, and CEP350 (Supplemental Table S1). Cilium dismantling induces premature MuSCs activation, reduces MuSCs self-renewal, and increases Myogenin expression [93 94-97]. These phenomena were also observed in *Ezh1*$^{-/-}$ MuSCs (Figure 4). We interrogated Ezh1 binding at selected cilium genes and found that Ezh1 occupies both the Arl13b and the IFT88 genes (Figure 6D). These findings suggested a potential regulatory role of Ezh1 on cilium formation or maintenance. Therefore, we used Pax7, Arl13b, and acetylated α-tubulin antibodies to identify ciliated MuSCs (Figure 6E). Muscle sections of either resting or regenerating *Ezh1*$^{-/-}$ mice had a lower percentage of ciliated MuSCs compared to WT (Figure 6F). This phenomenon was also evident in myofiber-associated MuSCs, with *Ezh1*$^{-/-}$ myofibers displaying fewer ciliated MuSCs than WT when assessed immediately after isolation (t0) or after being cultured for 72 hrs (t72) (Figure 6G). The primary cilium is the central organelle for the transduction of Hedgehog (Hh) signaling pathway in vertebrates [93,98]. Sonic Hh promotes Smoothened (SMO) to enter the cilium, thereby relieving repression of the Gli transcription factors [99]. To probe for Hh signaling, we used the small molecule SMO agonist SAG1.3 [100]. Gli1, Gli2, and Ptch1 expression was reduced in *Ezh1*$^{-/-}$ MuSCs. SAG1.3 treatment of WT MuSCs promptly activated Gli1, Gli2, and Ptch1 but failed to fully restore their expression in *Ezh1*$^{-/-}$ MuSCs (Figure 6H). Overall, these findings indicate that Ezh1 may regulate expression of members of the Notch pathway and of critical components of the primary cilium in MuSCs.

NICD rescues the loss of MuSCs and re-establishes MuSCs ciliation in *Ezh1*$^{-/-}$ mice

Impaired expression of the Notch pathway in *Ezh1*$^{-/-}$ MuSCs, rescued Notch reported activity by exogenously provided Ezh1 in *Ezh1*$^{-/-}$ myoblasts, and binding of Ezh1 at genomic regulatory regions of Notch downregulated genes prompted us to evaluate whether Ezh1 may directly control Notch targets. To this end, we transfected a Notch reporter luciferase construct (multimerized CBF1-luc) with Notch intracellular domain (NICD) and Ezh1 expression vectors into C2C12 myogenic cells. Following proteolytic cleavage, the Notch intracellular domain (NICD) translocates to the nucleus and activates gene expression [101-103]. As expected, NICD activated the Notch reporter construct. Increasing amounts of transfected Ezh1 expression vector progressively augmented NICD-mediated transactivation of the Notch reporter (Figure 7A,B). Ezh1 harbors a hidden, partially disordered acidic transactivation domain capable of interacting with the p300 acetyltransferase and activating gene expression [104]. We tested whether endogenous Ezh1 and p300 proteins may interact in cell extracts derived from C2C12 cells and found that p300 antibodies co-immunoprecipitated Ezh1 and, reciprocally, Ezh1 antibodies co-immunoprecipitated p300 (Figure 7C). These findings encouraged us to test whether re-establishing defective Notch signaling in MuSCs may correct the *Ezh1*$^{-/-}$ phenotype. Tamoxifen-inducible *Pax7*^{CreERT2}; *ROSA26*$^{STOP\text{-}NICD\text{-}GFP}$ mice expressing NICD and GFP were crossed with either WT or *Ezh1*$^{-/-}$ mice (Figure 7D). The resulting mice were treated with tamoxifen, injured

twice and then analyzed at 28 days post-2nd injury. In contrast to *Ezh1*$^{-/-}$ mice, which displayed a reduced number of Pax7^{+} and Pax7^{+}/Arl13b^{+} cells (Figure 4C and Figure 6D), muscle sections derived from WT *Pax7*^{CreERT2}; *ROSA26*$^{STOP\text{-}NICD\text{-}GFP}$ or *Pax7*^{CreERT2}; *ROSA26*$^{STOP\text{-}NICD\text{-}GFP}$; *Ezh1*$^{-/-}$ mice revealed comparable numbers of Pax7^{+} and Pax7^{+}/Arl13b^{+} cells (Figure 7 E,F). Hes1 expression, which was reduced in *Ezh1*$^{-/-}$ MuSCs (Figure 1 and Figure 6), was restored in *Pax7*^{CreERT2}; *ROSA26*$^{STOP\text{-}NICD\text{-}GFP}$; *Ezh1*$^{-/-}$ mice (Figure 7G). Cross-sectional area could not be evaluated as NICD overexpression interferes with muscle regeneration [75,105]. EdU incorporation and MyoD expression, which were increased in *Ezh1*$^{-/-}$ MuSCs (Figure 2 H,I), were comparable in myofiber-associated MuSCs of *Pax7*^{CreERT2}; *ROSA26*$^{STOP\text{-}NICD\text{-}GFP}$ and Pax7^{CreERT2}; *ROSA26*$^{STOP\text{-}NICD\text{-}GFP}$; *Ezh1*$^{-/-}$ mice (Figure 7H,I). Thus, re-establishing Notch signaling in *Ezh1*$^{-/-}$ MuSCs mice restored the number of MuSCs, corrected their ciliation defects, and prevented premature MuSCs activation.

Discussion

Multiple regulatory layers safeguard cell quiescence [106]. Redundant mechanisms preserving quiescence may be critical for tissues and organs with few long-lived adult stem cells, such as skeletal muscle and brain, to shield them from unintended cell activation and consequent depletion. Dysregulation of such mechanisms results in defective stem cells. For instance, while old neuronal stem cells are refractory to activation, MuSCs are spontaneously activated during aging, accounting for the loss of MuSCs observed in old mice and elderly individuals [15,57,58,107-109]. The balance between cell quiescence and activation is a finely-tuned process that depends on transcriptional and epigenetic regulators, non-coding RNAs, translational modifications, metabolic switches, and local and systemic cues control the balance between cell quiescence and activation [19,110-112]. Polycomb group proteins participate in this regulation by exerting multiple functions. Genetic deletion of the PRC2 *Phf19* subunit increases identity and quiescence of hematopoietic stem cells (HSCs) [113] whereas ablation of PRC2 *Ezh1* impairs self-renewal and induces HSCs senescence [114]. Ezh1 repression also favors generation of iPSC-derived T cells [115]. These findings indicate that both protein complex composition and cellular environment are critical determinants of PRC2 activity [116]. Even within the same cell type (i.e., HSCs), Ezh1 can either repress or activate transcription of distinct sets of genes [86]. These contrasting transcriptional properties may be reconciled by the observation that Ezh1 and Ezh2 each contain a locked and buried partially disordered acidic transcriptional activation domain (TAD) capable of activating gene expression. The SANT1-Binding Domain (SBD) of Ezh1 displays lower binding affinity to the SANT1 domain compared to that of Ezh2, making the Ezh1 TAD potentially more accessible for the binding to active transcriptional machineries [47,104]. PRC2 *Ezh2* inactivation in MuSCs impairs their proliferation and derepresses expression of non-myogenic lineage genes [27,28]. Here, we observed neither proliferation defects nor lineage-specific gene derepression in *Ezh1*$^{-/-}$ MuSCs. Rather, we found that *Ezh1*$^{-/-}$ MuSCs were spontaneously activated and prematurely differentiated both in culture and in regenerating mice. H3K27me3, a PRC2 hallmark which is decreased in *Ezh2*$^{-/-}$ MuSCs [27,28], was not modified in *Ezh1*$^{-/-}$ MuSCs. Ezh1 was expressed in quiescent MuSCs whereas Ezh2 is only detected in activated MuSCs [27,42]. Altogether, their expression profile,

distinct epigenetic landmarks, and functional phenotypes indicate that Ezh1 and Ezh2 are not redundant and have different functions in MuSCs. Specifically, Ezh1 maintains MuSCs quiescence while Ezh2 is required for MuSC activation. We also observed that expression of several members of the Notch pathways was reduced in *Ezh1*$^{-/-}$ MuSCs. Notch signalling is required for MuSCs quiescence as abrogation of canonical Notch signaling results in spontaneous MuSCs activation and differentiation [70,71]. Precocious MuSCs differentiation occurs upon germline or conditional deletion of Pax7 [117,118], and either Pax7 deletion or Notch signaling abrogation leads to loss of MuSCs. Ectopic expression of the active intracellular domain of Notch1 rescues the loss of Pax7$^{-/-}$ MuSCs and restores their proliferation potential [105]. Moreover, both Ezh1 and Notch are reduced in precociously differentiating aged MuSCs [56 119]. In *Ezh1*$^{-/-}$ mice, we observed spontaneous MuSCs activation and early differentiation with consequent reduction of the number of Pax7^{+} cells and impaired regeneration. The percentage of ciliated *Ezh1*$^{-/-}$ MuSCs was also decreased. Cilium dismantling induces premature MuSCs activation, reduces MuSCs self-renewal, and increases Myogenin expression [94,95], effects that were also observed in *Ezh1*$^{-/-}$ MuSCs. A role for the primary cilium in Notch signaling has been reported in epidermal cells [120]. In endothelial cells, Ezh1 promotes transcription of the Notch ligand Dll4 [51] and in zebrafish Ezh1 enhances Notch signaling to activate arterial gene expression [121]. We cannot formally exclude that Ezh1 may regulate MuSCs quiescence and indirectly affect the Notch pathway. However, the following observations support a direct role of Ezh1 in the regulation of the Notch pathway: i) Ezh1 was found at regulatory regions of Notch signaling members ; ii) transfection experiments revealed a coactivatory role of Ezh1 on NICD-mediated gene transcription; iii) exogenously supplied Ezh1 could restore expression driven by a Notch reporter in *Ezh1*$^{-/-}$ myoblasts. Furthermore, re-establishing Notch signaling by NICD ectopic expression in MuSCs resulted in a comparable increase of total and ciliated Pax7^{+} cells in both WT and *Ezh1*$^{-/-}$ mice. Notch signaling components are enriched in the primary cilia of suprabasal epidermal cells, and differentiation defects in ciliary mutants mice could also be rescued by NICD expression [120]. Overall, this study reveals a critical role for Polycomb Ezh1 in maintaining MuSCs quiescence and is consistent with a non-canonical function to Polycomb proteins in the regulation of Notch signalling.

Limitations of the study

The *Ezh1*$^{-/-}$ mice used in this study are total body knock-out. Even though transplantation experiments and selective reconstitution of the Notch signaling indicate a cell autonomous role of Ezh1 in MuSCs, we cannot formally exclude the possibility that other cell lineages may contribute to the observed phenotypes. Further, the high specificity but low affinity of the antibodies used (and the low specificity of commercially available antibodies) have precluded an analysis of the genome-wide distribution of Ezh1.

STAR Methods

RESOURCE AVAILABILITY

Lead Contact—Vittorio Sartorelli (Vittorio.Sartorelli@nih.gov).

Materials Availability—Further information and requests for resources and reagents should be directed to and will be fulfilled by the Lead Contact. This study did not generate new unique reagents.

Data and Code Availability—Any additional information required to reanalyze the data reported in this work paper is available from the Lead Contact upon request

EXPERIMENTAL MODEL AND SUBJECT DETAILS

Mice—Ezh1-null mice (*Ezh1*$^{-/-}$) (https://www.informatics.jax.org/allele/MGI:4941012) were generated at the Research Institute of Molecular Pathology (IMP, Vienna) by Dr. Donal O'Carroll (laboratory of Dr. Thomas Jenuwein) with the help of Dr. Maria Sibilia (laboratory of Erwin Wagner), were described in [44], and were obtained from Dr. Lothar Hennighausen (NIDDK, NIH). *Ezh1*$^{-/-}$ mice were backcrossed with C57BL/6J more than 6 generations before being bred back to homozygosity. C57BL/6J (JAX: 000664); tamoxifen inducible *Pax7*^{CreERT2} (JAX: 017763) [81]; nuclear membrane binding *ROSA26*$^{STOP\text{-}Sun\text{-}1\text{-}GFP}$ (JAX: 021039) [82] and immunodeficient NRG (NOD-*Rag1*^{null} *IL2rg*^{null}) (JAX: 007799) mice were imported from the Jackson Laboratory. *ROSA26*$^{STOP\text{-}NICD\text{-}GFP}$ (JAX: 008159) mice were obtained from Dr. Keisuke (Chris) Nagao's lab (NIAMS, NIH). *Pax7*^{CreERT2} and *ROSA26*$^{STOP\text{-}Sun\text{-}1\text{-}GFP}$ mice were intercrossed to generate *Pax7*^{CreERT2} ; *ROSA26*$^{STOP\text{-}Sun\text{-}1\text{-}GFP}$ mice. *Pax7*^{CreERT2} ; *ROSA26*$^{STOP\text{-}Sun\text{-}1\text{-}GFP}$ were further intercrossed with *Ezh1*$^{-/-}$ mice to generate *Pax7*^{CreERT2} ; *ROSA26*$^{STOP\text{-}Sun\text{-}1\text{-}GFP}$; *Ezh1*$^{-/-}$mice. For comparative studies, age and sex were matched in each setting. Genotyping was done by a TaqMan based genotyping approach provided by Transnetyx Inc (http://www.transnetyx.com). Mice were housed in a pathogen-free facility and all experiments were performed according to the National Institutes of Health (NIH) Animal Care and Use regulations. Housing conditions: temperature ~72F (~22°C, 40-60% humidity, 14/10 light/dark daily cycle.

METHOD DETAILS

MuSCs isolation by FACS—A single-cell suspension of MuSCs was prepared as previously described (Riparini et al, 2022). Briefly, hindlimb muscles of adult wild-type mice (3- to 6-month-old) were mechanically minced and enzymatically digested with collagenase II (1000U/ml) for 1 hr at 37 °C in Ham's F10 containing 10% horse serum. The resulting muscle slurry was further digested with a mixture of collagenase II/dispase for an additional 30 min at 37 °C. The digested suspension was passed 10 times through a 20-gauge needle syringe and the single cell suspension was then filtered with a 40-μm cell strainer to eliminate debris. Cells were incubated with the following primary antibodies: APC anti-mouse CD31 (BioLegend 102510; 1:100), APC anti-mouse CD45 (BioLegend 103112; 1:100), Pacific Blue anti-mouse Ly-6A/E (anti-Sca1, BioLegend 108120; 1:100), biotin anti-mouse CD106 (anti-VCAM1, BioLegend 105703; 1:50), PE-Cy7 Streptavidin (BioLegend 405206; 1:100), PE-α7-Integrin (clone:R2F2, The University of British Columbia 53-0010-01, 1:250). 7-AAD (ThermoFisher Scientific A1310, 1:1000) was used to identify living cells. MuSCs were identified as CD31−/CD45−/Scal−/VCAM-1+/α7-Integrin+ events.

MuSC transplantation—One day before transplantation, NRG mice were injured with 2 μm notexin solution on the right hindlimb TA/EDL muscles. Approximately 3 X 10^4 FACS-isolated MuSCs obtained from either *Pax7*^{CreERT2} ; *R26-*$^{STOP\text{-}Sun\text{-}1\text{-}GFP}$ or *Pax7*^{CreERT2} ; *R26-*$^{STOP\text{-}Sun\text{-}1\text{-}GFP}$; *Ezh1*$^{-/-}$ mice were resuspended in 100ul of 1xPBS, and transplanted by intramuscular injection with a Hamilton syringe into pre-injured TA/EDL muscles of each NRG mouse. Transplanted mice were allowed to recover for 28 days under normal husbandry. On day 28 after the first injury, the transplanted mice were subjected to another round of muscle injury and allowed to recover for additional 28 days, after which they were euthanized. The injured/cell transplanted TA/EDL were collected for cryo embedding, sectioning and immunofluorescence assay.

MuSCs size measurements and time-lapse microscopy—Immediately after FACS isolation, 1-1.5 X 10^5 MuSCs were seeded onto a Ibidi μ-Slide 8-well plate and incubated for 15 min at 37°C. After 15 min, fresh medium was added and cells were immediately placed in the IncuCyte S3 Live-Cell Analysis System (Essen BioScience) for phase-contrast live image microscopy for 60hr. ImageJ 1.53a was used for the quantification of the area (μm^2) of individual cells captured every 15 min of incubation in the IncuCyte. Non-aggregated single cells were selected for cell size quantification. Cell size was also determined by FACS forward scatter (FSC) intensity which is proportional to the diameter of the cell [122].

Movies were obtained from WT and *Ezh1*$^{-/-}$ MuSCs and the time-to-first division was manually calculated in individual cells. The “time to first division” was determined to be the time point prior to the division into 2 daughter cells.

Primary myoblasts isolation and culture—Primary myoblasts (PM) derived from 3-4-month-old WT or *Ezh1*$^{-/-}$ mice were isolated following described methods [123,124]. Briefly, hindlimbs muscle were dissociated into single cells by enzymatic digestion with collagenase II (1000 U/ml) in Ham’s F10 medium, supplemented with 10% horse serum and 1% penicillin and streptomycin (wash medium) at 37°C for 60 min. Digested muscles were then subjected to further digestion with collagenase II (1000 U/ml) and dispase (11 U/ml) for 30 min. Cell suspension was then plated on 10 cm plate and incubated overnight at 37° C 5% CO_2. The following day primary myoblasts were enriched by pre-plating. Suspended cells were pre-plated twice for 2hr in 10 cm plate, collected by centrifugation and plated in 10 cm collagen coated dish. When cells reached 70-80% confluency, they were removed from the plate, using PBS and enriched by pre-plating for 30 min in 10 cm collagen coated dish. Suspended cells were then seeded at a density 1 X 10^4 cells/cm^2. Primary myoblasts were cultured in medium supplemented with 2.5 ng/ml bFGF.

Mice tamoxifen treatment and *in vivo* EdU chasing—A solution of 10 mg/mL tamoxifen was prepared in corn oil and stored at 4°C. 2 mg (~ 200 μL) tamoxifen was delivered intraperitoneally (IP) daily for 5 consecutive days for each mouse. For *in vivo* EdU chasing, after tamoxifen induction, *Pax7*^{CreERT2} ; *R26-*$^{STOP\text{-}Sun\text{-}1\text{-}GFP}$ and *Pax7*^{CreERT2} ; *R26-*$^{STOP\text{-}Sun\text{-}1\text{-}GFP}$; *Ezh*$^{-/-}$ mice were subjected to EdU IP injection daily for 14 consecutive days.

Briefly, EdU was prepared at 20 mg/mL in saline solution and 6 mg EdU (~300 μL) was delivered IP daily to each mouse. Mice were sacrificed on day 15, TA/EDL muscles were collected and cryo-embedded in OCT in a methylbutane bath. Muscles were further sectioned and analyzed by immunofluorescence and confocal imaging.

Muscle injury—Mice were anesthetized in an Isoflurane Scavenging System with appropriate pain relief measure (IP injection; 100 μL Buprenorphine (0.3mg/mL) for each mouse). One limb was wiped with 70% alcohol pad to sanitize the skin. A small incision was introduced around the TA/EDL muscles and 50-100 μL notexin (2 μg/mL) were injected into the TA/EDL muscles with an insulin syringe. For a second injury, the mice were allowed to recover for twenty-eight (28) days between injuries. Wound clips were applied to suture the small skin opening that exposed the TA/EDL muscles and subsequently removed at day 3 or 5 post injury.

Muscle dissection, cryo-embedding, and sectioning—The TA/EDL muscles obtained from uninjured (resting) or injured mice were processed three, seven or twenty-eight days after 1st or 2nd rounds of muscle injury. The TA/EDL muscles were dissected, snap-frozen in cold methylbutane with OCT cover. Cryo-embedded tissues were mounted on a Leica cryostat in transverse direction and sectioned at 10 μm thickness. Cryo-sections were collected by adhering to frosted slides (positive charged) and air dried for at least 10 min before being processed immediately or stored long term at −80°C. For consistency, transverse cross sections 1.8-2.0 mm away from the knee side were collected for comparative studies. The details are described in [125].

Single muscle fiber isolation, culture, and EdU chasing—Isolated EDL muscles were placed in a 2 mL prewarmed single fiber digestion medium (2.5 mg/mL Collagenase type I in DMEM high glucose GIBCO cat. #11995-065) at 33 °C and incubated for 1hr until fibers started to disassociate. The muscle was moved to a 6 cm petri dish containing wash medium (DMEM high glucose) and gently triturated under a dissecting microscope with a heat-polished glass Pasteur pipette treated with horse serum. Single fibers were gradually released and collected using a small bore sized Pasteur pipette to a new washing medium petri dish. Single fibers were either immediately fixed by 4% PFA or further cultured in culture medium (20% FBS, 1% CEE in DMEM) in a 5% CO_2 tissue culture incubator. 60-100 single fibers from 4 mice were quantified. Single fibers were collected 24hr after culture and fixed with 4% PFA. For EdU incorporation studies, single fibers were cultured for 24hr, incubated with EdU (10mM) at 1:1000 dilution for additional 4hr, collected, and fixed with 4% PFA. Fixed muscle fibers were washed with 1x PBS for 5 min three times and stored at 4 °C for subsequent immunofluorescence and Click-iT EdU assay. Single fibers for studying ciliated Pax7^{+} cells were cultured for 72hr (t72) and fixed with 4% PFA.

Immunofluorescence of muscle cryo-sections and single fibers—Muscle sections on the approximately same axial level were subjected to immunofluorescence with antibodies described in Supplemental Materials. A detailed immunofluorescence protocol for muscle sections is described in [125]. Briefly, muscle sections were fixed with 2% PFA for 5 min at room temperature and rinsed with 1x PBST for three times. Samples were

incubated with primary antibodies in blocking buffer (1x PBST with 2% BSA and 5% NGS), incubated for 1 hour at room temperature or over night at 4°C and rinsed with 1x PBST for three times. Secondary antibodies diluted in blocking buffer were applied for 40 min at room temperature and rinsed with 1x PBST for three times. The sections then were fixed with 4% PFA for 10 min, counterstained with DAPI for 10 min, and rinsed with 1x PBST for three times. For muscle single fibers, immunostaining was carried out either in a 12- well tissue culture plate or a 2-well ibidi μ-slide chamber slide. The antibody dilutions and development conditions were the same as that of muscle sections, except that washing buffer was 1x PBST-H (1x PBST with 5% horse serum). The secondary antibodies were chosen according to the primary antibody epitopes and mismatch with different Alexa dyes in double or triple immunofluorescence.

TUNEL and EdU Click-iT assay—Apoptosis assays were performed on muscle sections immunostained with Pax7 antibody by utilizing Click-iT Plus TUNEL Assay Alexa Fluor 594 (ThermoFisher cat#: C10618). Briefly, after Pax7 antibody immunofluorescence, samples were rinsed with 1x PBST for three time. 200 μL of TdT reaction mix was applied on the slide to cover all sections, incubated for 60 min at 37°C and rinsed with 1x PBST for three times. 200 μL Click-iT™ Plus TUNEL reaction cocktail was applied, incubated for 30 min at 37°C. Samples were treated with 4% PFA for 10 min, counter stained with DAPI for another 10 min, and mounted for imaging. Detailed cocktail components are described in the kit user manual. EdU Click-iT assay (ThermoFisher Cat: C10338) was performed on muscle sections of mice injected with EdU for 14 consecutive days and single muscle fibers that were incubated with EdU. For muscle sections, after light fixation with 2% PFA, the sections were rinsed with 1x PBST for three time. ~200 μL Click-iT reaction cocktail was added on each slide to cover all sections, incubated for 30 min at room temperature. Slides were rinsed with 1x PBST for three times, post fixed with 4% PFA for 10 min, and counterstained with DAPI for 10 min. For single fibers, the EdU Click-iT assay was performed following immunostaining of muscle fibers with Pax7 and/or GFP antibodies. Briefly, after immunostaining single fibers were placed in a 2-well ibidi μ-slide chamber slide with 1x PBST-H which was then replaced with 500 μL Click-iT reaction cocktail. Samples were incubated for 30 min at room temperature and rinsed with 1x PBST-H for three times and processed. Detailed cocktail components are described in the kit user manual.

Fiber Size Analysis, Cell Counting, and Immunofluorescence Quantification—Muscle cross sectional area (CSA) was automatically identified and calculated by Image Pro 9.2 software (Media Cybernetics Inc.). Approximately 1,000-1,500 myofibers/mouse were quantified (n=3 mice). $Pax7^+$, $MyoD^+$, $MyoG^+$, GFP^+, ciliated $Pax7^+$, EdU^+ were counted manually using Photoshop count tools. Hes1 immunofluorescence intensity was measured using ImageJ Fuji.

Collagen Staining—Muscle cryo-sections were rehydrated with ddH_20 for 5 min and fixed with 4% PFA for 30 min at room temperature. Slides were washed with ddH_20 twice. Picro Sirius Red Solution (Abcam, Cat# ab150681) was applied to completely cover the tissue sections for 60 min at room temperature. Slides were quickly rinsed in 2 changes

of acetic acid solution and once in absolute alcohol. Slides were dehydrated in 2 changes of absolute alcohol, soaked in Xylene and mounted for bright-field microscopy (ECHO Revolve) for imaging.

Imaging—Immunofluorescence images were acquired either on Carl Zeiss LSM780 confocal microscope or Leica DMR6000 wide field fluorescence microscope (for single fibers). For whole section image, the section was scanned by combined Z-stack and tiling functions with 5 focal planes on 8x10 tiling field under 20x magnification. The image was further projected and stitched into one focal plane, exported as a .tif file for analysis. For $Pax7^+$cell counting, the sections were scanned with Z-stack and 4x4 or 3x3 tiling on the middle of TA muscle under 20x magnification, the image was further projected and stitched into one focal plane and exported. For ciliated $Pax7^+$ cell assays, muscle sections were imaged under 100x magnification.

Transmission Electron Microscopy—Mouse hind leg muscles were dissected, rinsed with PBS and immersed in fixative (2.5% glutaraldehyde/2% formaldehyde/2 mM $CaCl_2$ in 0.1 M cacodylate buffer, pH 7.4) and fixed for 1.5 hour. Small blocks (< 1 mm^3) were cut out, post fixed by 2% OsO_4 in 0.1 M cacodylate buffer for pH 7.4 for 2hr and *end bloc* stained in 2% aqueous uranyl acetate overnight. Upon dehydration with series of ethanol concentrations and embedding in EMBed-812 (EM Science, Horsham, PA), the blocs were flat embedded and resin polymerized for 60hr at 60°C. Ultrathin (80 nm) sections were cut parallel to the muscle fibers using Leica EM UC7 microtome. Sections were mounted on formvar – carbon coated grids. Samples were viewed and images recorded on Thermo Fisher Scientific FEI Tecnai 20 transmission electron microscope operated at 120 kV and equipped with AMT XR 81 wide angle camera.

Smoothened agonist (SAG) treatment—Primary myoblasts derived from the hindlimbs of 2 to 4 -month-old C56BL/6J wild-type and *Ezh1*$^{-/-}$ mice were cultured for two passages in HAM's F10 supplemented with 2.5 ng/μL of bFGF, 10% horse serum, and penicillin and streptomycin (growth medium). Cells were plated at a density of 1000 cells/cm^2 in growth medium with either DMSO or 1uM SAG1.3. After 24hr cells were collected for downstream analysis.

Immunoblotting—MuSCs were lysed and their extracts resolved by SDS-PAGE, transferred into nitrocellulose membrane and immunoblotted with Ezh1 (Proteintech, 20852-1-AP) and GAPDH (Cell Signaling, #5174) antibodies. C2C12 cells were co-transfected with a Notch reporter construct (multimerized CBF1-luc) and plasmids expressing NICD1 and Myc-Ezh1. After 48 h, cells were collected in lysis buffer (20mM Tris-HCl [pH8.0], 10% glycerol, 150mM NaCl, 5mM MgCl2, 0.1% NP-40, protease inhibitors, phosphatase inhibitors). Total protein samples were separated on a NuPAGE 4-12% Bis-Tris Gel and transferred to a nitrocellulose membrane for immunoblotting with Myc (Millipore 05-419), NICD1 (NICD1, Abcam ab 52627), or Tubulin (DSHB #E7) antibodies. Cell extracts of primary myoblasts were processed and immunoblotted as descrived above for C2C12 cell extracts.

Immunoprecipitation—C2C12 cells were differentiated for 48hr, and harvested with lysis buffer (20 mM Tris–HCl (pH 8.0), 10% glycerol, 150 mM NaCl, 5 mM $MgCl_2$, 0.1% NP-40, protease and phosphatase inhibitors). 1 mg of whole cell lysate was incubated with mouse IgG (Cell Signaling #5415), anti-Ezh1 antibody (Cell Signaling #42088) or anti-p300 antibody (Active Motif #61401) and protein G-agarose (for IgG or p300 antibody) or protein-A agarose (for Ezh1 antibody) beads. Bound immunocomplexes were captured and eluted by heating in LDS sample buffer (Invitrogen), resolved on NuPAGE 4-12% Bis-Tris gel (Invitrogen), transferred to nitrocellulose membrane and subjected to immunoblotting with either anti-Ezh1 or anti-p300 antibody (1:1,000 dilution).

RT-qPCR—~1 X 10^5 primary myoblasts from WT or *Ezh1*$^{-/-}$ mice were collected in 1 mL TRIzol™ reagent (Thermo Fisher Inc.) and RNA reverse transcribed (RT) with High-Capacity cDNA Reverse Transcription Kit (Thermo Fisher Inc.). Real time quantitative PCR was performed with SYBR green PCR master mix (ThermoFisher Inc.). Relative quantification (fold change) for each gene transcript was calculated by ddCT method, using GAPDH as an internal control. The sequences of primers are provided in Supplemental Table S2 and STAR methods.

Plasmids, cell line, transient transfection and dual-luciferase assays—Lipofectamine 3000 (ThermoFisher) was used to transiently transfect a Notch luciferase reporter plasmid (multimerized CBF1-luc) [126], mammalian expression vectors pCAGGS-NICD (Addgene#26891) and pHAN-Myc-Ezh1 [47] into C2C12 cells obtained from ATCC (CRL-1772). C2C12 cells were cultured in DMEM supplemented with 20% FBS and induced to differentiate with DMEM supplemented with 2% horse serum, 1X insulin-transferrin-selenium. Primary myoblasts derived from either WT or *Ezh1*$^{-/-}$ mice were transfected with multimerized CBF1-luc reporter plasmid and/or pHAN-Myc-full length Ezh1 or pHAN-Myc-mutant Ezh1$^{\Delta SET}$ expression vectors [47]. pcDNA3 plasmid was used to normalize the total amount of plasmids in each transfection, and a *Renilla* luciferase reporter was used to calibrate transfection efficiency. Luciferase reporter assay was done using the Dual-luciferase reporter assay system (Promega). *Firefly* luciferase values were normalized by cotransfected *Renilla* luciferase values.

RNA-seq—For transcriptome analysis Illumina RNA libraries were prepared with NEBNext Ultra II RNA library preparation kit for Illumina (NEB #E7490) according to manufacturer's instructions. Briefly, 100 ng of total RNA were enriched for poly $(A)^+$ mRNA and retrotranscribed. cDNAs were then fragmented and adapters added to each end of the fragments. The obtained libraries were amplified, and size selected prior to NGS analysis. All libraries were diluted to 3nM and sequenced on an Illumina NovaSeq6000 or Illumina NextSeq550 using the following read length: 50bp for Read1, 8 bp for I7 Index, and 50 bp for Read2.

RNA-seq analysis—Raw sequencing data were demultiplexed and converted to with FastQ with bcl2fastq/2.17.1. After removing adapters using trimgalore/0.4.5 (https://github.com/FelixKrueger/TrimGalore), the reads were mapped to mm10 using TopHat 2.1.1 [127]. Partek Genomics Suite 7.18 (PGS) was used to calculate Reads Per Kilobase per Million

mapped reads (RPKM), perform analysis of variance (ANOVA) comparison, perform principal component analysis(PCA) and hierarchical analyisis. Downstream analyses were performed with customized R program (http://www.R-project.org/). Transcriptomes of activated (T3-T0; T5-T0; 5-T3) MuSCs are reported in [60].

scRNA-seq—Single-cell RNA-seq libraries were prepared using the Chromium Single Cell 3' Library & Gel Bead Kit v3.1 (P/N 1000121, 10x Genomics). GEM-RT was performed in a C1000 Touch Thermal cycler with 96-Deep Well Reaction Module (Bio-Rad; P/N 1851197): 53°C for 45 min, 85°C for 5 min; held at 4°C. Following retrotranscription, GEMs were broken, and the single-strand cDNA was purified with DynaBeads MyOne Silane Beads. cDNA was amplified using the C1000 Touch Thermal cycler with 96-Deep Well Reaction Module: 98°C for 3 min; cycled 12 times: 98°C for 15 s, 63°C for 20 s, and 72°C for 1 min; 72°C for 1 min; held at 4°C. Amplified cDNA product was purified with the SPRIselect Reagent Kit (0.6× SPRI). Indexed sequencing libraries were constructed using the reagents in the Chromium Single Cell 3' Library & Gel Bead Kit v2, The final libraries were diluted to 3 nM and sequenced on an Illumina NovaSeq6000 or Illumina NextSeq550 using the following read length: 28bp for Read1, 8 bp for I7 Index, and 91 bp for Read2.

scRNA-seq analysis—Sequences from the Chromium platform were de-multiplexed and aligned using CellRanger ver. 3.0.2 from 10x Genomics with default parameters (https://support.10xgenomics.com/single-cell-gene-expression/software/pipelines/latest/what-is-cell-ranger). For clustering, filtering, variable gene selection, dimensionality reduction are performed using the Seurat ver.4.1.0 [128,129]. The detailed After cells with fewer than 200 detected genes were excluded, cells with lower percentage of UMIs mapped to mitochondrial genes were collected. The UMI counts per million were log-normalized for each cell using the natural logarithm. Variable genes were selected using the thresholds after calculating the binned values from log average expression and dispersion for each gene. The expression level of highly variable genes was scaled along each gene, and cell-cell variation in gene expression was regressed out by the number of detected molecules, and mitochondrial gene expression. The scaled data were projected onto a low-dimensional subspace of PCA (principle component analysis) using dimensional reduction. The number of PCA were decided through the assessment of statistical plots. To correct for batch effects, datasets were integrated with cellranger aggr pipeline (https://support.10xgenomics.com/single-cell-gene-expression/software/pipelines/latest/using/aggregate). Cells were clustered using a graph-based clustering approach optimized by the Louvain algorithm with resolution parameters and visualized using two-dimensional UMAP (Uniform Manifold Approximation and Projection). Clusters identification was established by partitioning cells into distinct groups, based on DEGs, and subsequent annotation of each group to a a given cell type based on the distribution of specific gene markers. In addition, using the top-n markers based on log-fold changing values, we generated an expression heatmap for given cells and genes in the clusters.

Single-cell pseudotime analysis—Pseudotime analysis of scRNA (single cell RNA) was performed using Monocle v.3.1.0 [130-132]. First, datasets containing information of cell

differentiation were created using cell ids selected through Seurat package. Dimensional reduction was perfromed using UMAP method to visualize the dataset, cells were ordered by global gene expression levels and visualized by pseudotime. To illustrate trends of gene expression across pseudo time, heatmaps were generated to represent gene smooth expression curves.

ChIP-qPCR—Freshly FACS-isolated MuSCs (~ 5 X 10^6) were immediately crosslinked in 1% formaldehyde. Cells were then lysed in Farnham buffer (5 mM PIPES pH8.0, 85 mM KCl, 0.5% NP-40) and subsequently in RIPA buffer (1X PBS, 1% NP-40, 0.5% sodium deoxycholate, 0.1% SDS). Chromatin was sheared using ME220 AFA Focused Ultrasonicator (Covaris). Immunoprecipitation was done by incubating fragmented, cross-linked chromatin with coupled magnetic bead (Dynabeads Protein A, ThermoFisher)-antibody complex. Chromatin derived from ~ 2.5 X 10^6 MuSCs was immunoprecipiated with either control IgG (rabbit IgG, ab172730) or Ezh1 antibody (Ezh1-738) [47]. After overnight incubation, beads were washed successively in low salt buffer (20 mM Tris-HCl pH8.0, 150 mM NaCl, 2 mM EDTA, 0.1% SDS, 1% Triton X-100), high salt buffer (20 mM Tris-HCl pH8.0, 500 mM NaCl, 2 mM EDTA, 0.1% SDS, 1% Triton X-100), LiCl IP wash buffer (100 mM Tris-HCl pH7.5, 500 mM LiCl, 1% NP-40, 1% sodium deoxycholated) and 1X TE (10 mM Tris-HCl pH7.5, 0.1 mM EDTA). All washes were performed at 4°C for 5 mins. The eluted and purified ChIP DNA was subjected to real-time polymerase chain reaction using PowerUp SYBR Green Master Mix (ThermoFisher).

ChIP-seq—2.5-3.5 X 10^5 MuSCS were FACS-sorted and immediately crosslinked in 1% formaldehyde. Crosslinked cells were washed in 1X PBS, lysed in 250uL of RIPA buffer (1× PBS, 1% NP-40, 0.5% sodium deoxycholate, 0.1% SDS) and centrifuged at 2,000 rpm for 5 min. The chromatin fraction was shared by sonication with Covaris ME220. The resulting sheared chromatin was immunoprecipitated overnight. Immunoprecipitated DNA was then washed with the following buffers: Buffer I (20 mM Tris-HCl [pH 8.0], 150 mM NaCl, 2 mM EDTA, 0.1% SDS, 1% Triton X-100), Buffer II (20 mM Tris-HCl [pH 8.0], 500 mM NaCl, 2 mM EDTA, 0.1% SDS, 1% Triton X-100), Buffer III (10 mM Tris-HCl [pH 8.0] 250 mM LiCl, 1% NP-40; 1% sodium deoxycholate, 1 mM EDTA), and Tris-EDTA (pH 8.0). All washes were performed at 4°C for 3-5 min. Finally, crosslinking was reversed in elution buffer (100 mM NaHCO3, 1% SDS) at 65°C overnight. Immuno-precipitated DNA fragments were converted in ChIP-seq libraries with the NEBNext Ultra II DNA library prep kit for Illumina (New England Biolabs, (#E7645) following the manufacturer's protocol. Libraries were generated from MuSCs pooled from two (2) mice for each genotype per each replicate. Two males and two females mice of 12-16 weeks of age per each genotype were employed for each replicate (n=2). Final libraries were sequenced on NovaSeq6000 or NextSeq550 Illumina instrument using the following read length: 50bp for Read1, 8 bp for I7 Index, and 50 bp for Read2.

ChIP-seq analysis—ChIP-seq data were generated using Illumina NovaSeq6000 and NextSeq550 platforms. FastQ files were generated with ConfigureBclToFastq.pl (CASAVA-1.8.2). Adapter sequences were removed using cutadapt (https://cutadapt.readthedocs.io/en/stable/) and trimmed sequences aligned to the mm10 reference

genome using Bowtie/1.1.1 [133], allowing two mismatches. Uniquely mapped and non-redundant reads were used for peak calling with MACS 1.4.2 [134] with –p 1e-5 -B -S –nomodel or with SICER1.1 with W 200 G 600 FDR 0.05. Bigwig files were generated with BedGraphToBigWig [135] and Bedtools/2.19.1 [136]. Peak intensities were normalized as tags per 10 million reads (RP10M) in the original library. For genes identification, peaks were assigned to the closest TSS with HOMER/4.10.1. Intergenic H3K27me3 peaks were identified after excluding TSS and gene body peaks.

ATAC-seq—1.5-2.5 X 10^5 MuSCs were sorted in FACS medium and pelleted at 500g for 5 min in a 1.5mL Eppendorf tube. To tag and fragment accessible chromatin, cells were resuspended in 45uL of Transposition Reaction buffer: 25uL of 2X TD buffer (Illumina, Cat# FC-121-1030), 2.5 uL of TD enzyme (Illumina, Cat# FC-121-1030), 0.5uL of 1% Digitonin (Promega, Cat# G9441), 17uL of ddH2O. The transposition reaction was incubated at 37°C for 30 min with shaking at 300 rpm. Transposed DNA was immediately purified using Qiagen MinElute kit (Quiagen, Cat# 28106). DNA fragments were then barcoded and amplified by PCR (10–15 cycles based on the amplification curve). Final libraries were sequenced on NextSeq550 or NovaSeq6000 Illumina instrument using the following read length: 50bp for Read1, 8 bp for I7 Index, and 50 bp for Read2. ATAC-seq datasets for activated MuSCs are reported in [85].

ATAC-seq analysis—ATAC-seq data were generated using Illumina Hiseq2500 system. FastQ files were generated with ConfigureBclToFastq.pl (CASAVA-1.8.2). FastQ files were generated with bcl2fastq/2.17.1. Adapter sequences were removed using cutadapt/3.4 (https://cutadapt.readthedocs.io/en/stable). ATAC-seq reads from two biological replicates for each sample were mapped to mm10 genome using with Bowtie/1.1. [133]. Redundant reads were removed using FastUniq [137], and customized Python scripts were used to calculate the fragment length of each pair of uniquely mapped pair-end reads. The regions of open chromatin were identified by MACS 1.4.2 [134] with a p-value cutoff of 1.0E-05. Only regions called in both replicates were used in downstream analysis. Peak intensities were normalized as tags per 10 million reads(RP10M) in the original library. Peaks were assigned to the closest TSS with HOMER.

QUANTIFICATION AND STATISTICAL ANALYSIS

Values are presented as the mean ± standard deviation (represented as error bars) of three or more biological replicates. The sample size for separate experiment is stated in the corresponding figure legend. Statistical significance was tested using the unpaired two-sided Student’s t test. Results for which the test returned p-value of 0.05 or less were considered significant. Specific statistical parameters employed to analyze sequencing data are indicated in “Methods Details” section.

Supplementary Material

Refer to Web version on PubMed Central for supplementary material.

ACKNOWLEDGMENTS

We thank Keiko Sakamoto and Keisuke (Chris) Nagao (NIAMS, NIH) for sharing the *ROSA26*$^{STOP\text{-}NICD\text{-}GFP}$ mice. *Ezh1*$^{-/-}$ mice were generated at the Research Institute of Molecular Pathology (Vienna, Austria) by Donal O'Carroll (laboratory of Thomas Jenuwein) with the help of Maria Sibilia (laboratory of Erwin Wagner) and provided by the laboratory of Lothar Henninghausen (NIDDK, NIH). The Genomic Tehcnology Section, the Light Imaging Section, the Biodata Mining and Discovery Section, and the Flow Cytometry Section of the NIAMS-IRP provided assistance with experiments and data analysis. We thank Megan Laycock for manuscript editing. This work was supported in part by the Intramural Research Program of the NIAMS at the NIH (grants AR041126and AR041164 to V.S.).

INCLUSION AND DIVERSITY

One or more of the authors of this paper received support from a program designed to increase minority representation in science.

BIBLIOGRAPHY

1. Post Y, and Clevers H (2019). Defining Adult Stem Cell Function at Its Simplest: The Ability to Replace Lost Cells through Mitosis. Cell Stem Cell 25, 174–183. 10.1016/j.stem.2019.07.002. [PubMed: 31374197]
2. Yin H, Price F, and Rudnicki MA (2013). Satellite cells and the muscle stem cell niche. Physiol Rev 93, 23–67. 10.1152/physrev.00043.2011. [PubMed: 23303905]
3. Pawlikowski B, Pulliam C, Betta ND, Kardon G, and Olwin BB (2015). Pervasive satellite cell contribution to uninjured adult muscle fibers. Skelet Muscle 5, 42. 10.1186/s13395-015-0067-1. [PubMed: 26668715]
4. Keefe AC, Lawson JA, Flygare SD, Fox ZD, Colasanto MP, Mathew SJ, Yandell M, and Kardon G (2015). Muscle stem cells contribute to myofibres in sedentary adult mice. Nat Commun 6, 7087. 10.1038/ncomms8087. [PubMed: 25971691]
5. Almada AE, and Wagers AJ (2016). Molecular circuitry of stem cell fate in skeletal muscle regeneration, ageing and disease. Nat Rev Mol Cell Biol 17, 267–279. 10.1038/nrm.2016.7. [PubMed: 26956195]
6. Fuchs E, and Blau HM (2020). Tissue Stem Cells: Architects of Their Niches. Cell Stem Cell 27, 532–556. 10.1016/j.stem.2020.09.011. [PubMed: 33007238]
7. Sousa-Victor P, Garcia-Prat L, and Munoz-Canoves P (2022). Control of satellite cell function in muscle regeneration and its disruption in ageing. Nat Rev Mol Cell Biol 23, 204–226. 10.1038/s41580-021-00421-2. [PubMed: 34663964]
8. Kuang S, Kuroda K, Le Grand F, and Rudnicki MA (2007). Asymmetric self-renewal and commitment of satellite stem cells in muscle. Cell 129, 999–1010. 10.1016/j.cell.2007.03.044. [PubMed: 17540178]
9. Rodgers JT, King KY, Brett JO, Cromie MJ, Charville GW, Maguire KK, Brunson C, Mastey N, Liu L, Tsai CR, et al. (2014). mTORC1 controls the adaptive transition of quiescent stem cells from G0 to G(Alert). Nature 510, 393–396. 10.1038/nature13255. [PubMed: 24870234]
10. Sambasivan R, and Tajbakhsh S (2015). Adult skeletal muscle stem cells. Results Probl Cell Differ 56, 191–213. 10.1007/978-3-662-44608-9_9. [PubMed: 25344672]
11. van Velthoven CTJ, and Rando TA (2019). Stem Cell Quiescence: Dynamism, Restraint, and Cellular Idling. Cell Stem Cell 24, 213–225. 10.1016/j.stem.2019.01.001. [PubMed: 30735649]
12. Relaix F, Bencze M, Borok MJ, Der Vartanian A, Gattazzo F, Mademtzoglou D, Perez-Diaz S, Prola A, Reyes-Fernandez PC, Rotini A, and Taglietti t. (2021). Perspectives on skeletal muscle stem cells. Nat Commun 12, 692. 10.1038/s41467-020-20760-6. [PubMed: 33514709]
13. Murach KA, Fry CS, Dupont-Versteegden EE, McCarthy JJ, and Peterson CA (2021). Fusion and beyond: Satellite cell contributions to loading-induced skeletal muscle adaptation. FASEB J 35, e21893. 10.1096/fj.202101096R. [PubMed: 34480776]

14. Sacco A, Doyonnas R, Kraft P, Vitorovic S, and Blau HM (2008). Self-renewal and expansion of single transplanted muscle stem cells. Nature 456, 502–506. 10.1038/nature07384. [PubMed: 18806774]
15. Kalamakis G, Brune D, Ravichandran S, Bolz J, Fan W, Ziebell F, Stiehl T, Catala-Martinez F, Kupke J, Zhao S, et al. (2019). Quiescence Modulates Stem Cell Maintenance and Regenerative Capacity in the Aging Brain. Cell 176, 1407–1419 e1414. 10.1016/j.cell.2019.01.040. [PubMed: 30827680]
16. Florian MC, Nattamai KJ, Dorr K, Marka G, Uberle B, Vas V, Eckl C, Andra I, Schiemann M, Oostendorp RA, et al. (2013). A canonical to non-canonical Wnt signalling switch in haematopoietic stem-cell ageing. Nature 503, 392–396. 10.1038/nature12631. [PubMed: 24141946]
17. Cheung TH, and Rando TA (2013). Molecular regulation of stem cell quiescence. Nat Rev Mol Cell Biol 14, 329–340. 10.1038/nrm3591. [PubMed: 23698583]
18. Feige P, Brun CE, Ritso M, and Rudnicki MA (2018). Orienting Muscle Stem Cells for Regeneration in Homeostasis, Aging, and Disease. Cell Stem Cell 23, 653–664. 10.1016/j.stem.2018.10.006. [PubMed: 30388423]
19. Urban N, and Cheung TH (2021). Stem cell quiescence: the challenging path to activation. Development 148. 10.1242/dev.165084.
20. Escobar TM, Loyola A, and Reinberg D (2021). Parental nucleosome segregation and the inheritance of cellular identity. Nat Rev Genet 22, 379–392. 10.1038/s41576-020-00312-w. [PubMed: 33500558]
21. Reinberg D, and Vales LD (2018). Chromatin domains rich in inheritance. Science 361, 33–34. 10.1126/science.aat7871. [PubMed: 29976815]
22. Margueron R, and Reinberg D (2011). The Polycomb complex PRC2 and its mark in life. Nature 469, 343–349. 10.1038/nature09784. [PubMed: 21248841]
23. Brand M, and Dilworth FJ (2017). Splicing of Ezh1 gets muscle out of stressful situations. Nat Struct Mol Biol 24, 435–437. 10.1038/nsmb.3406. [PubMed: 28471428]
24. Schuettengruber B, Bourbon HM, Di Croce L, and Cavalli G (2017). Genome Regulation by Polycomb and Trithorax: 70 Years and Counting. Cell 171, 34–57. 10.1016/j.cell.2017.08.002. [PubMed: 28938122]
25. Yu JR, Lee CH, Oksuz O, Stafford JM, and Reinberg D (2019). PRC2 is high maintenance. Genes Dev 33, 903–935. 10.1101/gad.325050.119. [PubMed: 31123062]
26. Brand M, Nakka K, Zhu J, and Dilworth FJ (2019). Polycomb/Trithorax Antagonism: Cellular Memory in Stem Cell Fate and Function. Cell Stem Cell 24, 518–533. 10.1016/j.stem.2019.03.005. [PubMed: 30951661]
27. Juan AH, Derfoul A, Feng X, Ryall JG, Dell'Orso S, Pasut A, Zare H, Simone JM, Rudnicki MA, and Sartorelli V (2011). Polycomb EZH2 controls self-renewal and safeguards the transcriptional identity of skeletal muscle stem cells. Genes Dev 25, 789–794. 10.1101/gad.2027911. [PubMed: 21498568]
28. Woodhouse S, Pugazhendhi D, Brien P, and Pell JM (2013). Ezh2 maintains a key phase of muscle satellite cell expansion but does not regulate terminal differentiation. J Cell Sci 126, 565–579. 10.1242/jcs.114843. [PubMed: 23203812]
29. Ezhkova E, Pasolli HA, Parker JS, Stokes N, Su IH, Hannon G, Tarakhovsky A, and Fuchs E (2009). Ezh2 orchestrates gene expression for the stepwise differentiation of tissue-specific stem cells. Cell 136, 1122–1135. [PubMed: 19303854]
30. Su IH, Basavaraj A, Krutchinsky AN, Hobert O, Ullrich A, Chait BT, and Tarakhovsky A (2003). Ezh2 controls B cell development through histone H3 methylation and Igh rearrangement. Nat Immunol 4, 124–131. [PubMed: 12496962]
31. Yang XP, Jiang K, Hirahara K, Vahedi G, Afzali B, Sciume G, Bonelli M, Sun HW, Jankovic D, Kanno Y, et al. (2015). EZH2 is crucial for both differentiation of regulatory T cells and T effector cell expansion. Sci Rep 5, 10643. 10.1038/srep10643. [PubMed: 26090605]
32. Feng X, Juan AH, Wang HA, Ko KD, Zare H, and Sartorelli V (2016). Polycomb Ezh2 controls the fate of GABAergic neurons in the embryonic cerebellum. Development 143, 1971–1980. 10.1242/dev.132902. [PubMed: 27068104]

33. Pereira JD, Sansom SN, Smith J, Dobenecker MW, Tarakhovsky A, and Livesey FJ (2010). Ezh2, the histone methyltransferase of PRC2, regulates the balance between self-renewal and differentiation in the cerebral cortex. Proc Natl Acad Sci U S A 107, 15957–15962. 10.1073/pnas.1002530107. [PubMed: 20798045]
34. O'Carroll D, Erhardt S, Pagani M, Barton SC, Surani MA, and Jenuwein T (2001). The polycomb-group gene Ezh2 is required for early mouse development. Mol Cell Biol 21, 4330–4336. [PubMed: 11390661]
35. Pasini D, Bracken AP, Jensen MR, Lazzerini Denchi E, and Helin K (2004). Suz12 is essential for mouse development and for EZH2 histone methyltransferase activity. Embo J 23, 4061–4071. [PubMed: 15385962]
36. Shen X, Liu Y, Hsu YJ, Fujiwara Y, Kim J, Mao X, Yuan GC, and Orkin SH (2008). EZH1 Mediates Methylation on Histone H3 Lysine 27 and Complements EZH2 in Maintaining Stem Cell Identity and Executing Pluripotency. Mol Cell 32, 491–502. [PubMed: 19026780]
37. Collinson A, Collier AJ, Morgan NP, Sienerth AR, Chandra T, Andrews S, and Rugg-Gunn PJ (2016). Deletion of the Polycomb-Group Protein EZH2 Leads to Compromised Self-Renewal and Differentiation Defects in Human Embryonic Stem Cells. Cell Rep 17, 2700–2714. 10.1016/j.celrep.2016.11.032. [PubMed: 27926872]
38. Chiacchiera F, Rossi A, Jammula S, Zanotti M, and Pasini D (2016). PRC2 preserves intestinal progenitors and restricts secretory lineage commitment. EMBO J 35, 2301–2314. 10.15252/embj.201694550. [PubMed: 27585866]
39. Radulovic V, de Haan G, and Klauke K (2013). Polycomb-group proteins in hematopoietic stem cell regulation and hematopoietic neoplasms. Leukemia 27, 523–533. 10.1038/leu.2012.368. [PubMed: 23257781]
40. Mu W, Starmer J, Shibata Y, Yee D, and Magnuson T (2017). EZH1 in germ cells safeguards the function of PRC2 during spermatogenesis. Dev Biol 424, 198–207. 10.1016/j.ydbio.2017.02.017. [PubMed: 28254491]
41. Loh CH, and Veenstra GJC (2022). The Role of Polycomb Proteins in Cell Lineage Commitment and Embryonic Development. Epigenomes 6. 10.3390/epigenomes6030023.
42. Boonsanay V, Zhang T, Georgieva A, Kostin S, Qi H, Yuan X, Zhou Y, and Braun T (2016). Regulation of Skeletal Muscle Stem Cell Quiescence by Suv4-20h1-Dependent Facultative Heterochromatin Formation. Cell stem cell 18, 229–242. 10.1016/j.stem.2015.11.002. [PubMed: 26669898]
43. Margueron R, Li G, Sarma K, Blais A, Zavadil J, Woodcock CL, Dynlacht BD, and Reinberg D (2008). Ezh1 and Ezh2 maintain repressive chromatin through different mechanisms. Mol Cell 32, 503–518. 10.1016/j.molcel.2008.11.004. [PubMed: 19026781]
44. Ezhkova E, Lien WH, Stokes N, Pasolli HA, Silva JM, and Fuchs E (2011). EZH1 and EZH2 cogovern histone H3K27 trimethylation and are essential for hair follicle homeostasis and wound repair. Genes & development 25, 485–498. 10.1101/gad.2019811. [PubMed: 21317239]
45. Son J, Shen SS, Margueron R, and Reinberg D (2013). Nucleosome-binding activities within JARID2 and EZH1 regulate the function of PRC2 on chromatin. Genes Dev 27, 2663–2677. 10.1101/gad.225888.113. [PubMed: 24352422]
46. Stojic L, Jasencakova Z, Prezioso C, Stutzer A, Bodega B, Pasini D, Klingberg R, Mozzetta C, Margueron R, Puri PL, et al. (2011). Chromatin regulated interchange between polycomb repressive complex 2 (PRC2)-Ezh2 and PRC2-Ezh1 complexes controls myogenin activation in skeletal muscle cells. Epigenetics Chromatin 4, 16. 10.1186/1756-8935-4-16. [PubMed: 21892963]
47. Mousavi K, Zare H, Wang AH, and Sartorelli V (2012). Polycomb protein Ezh1 promotes RNA polymerase II elongation. Mol Cell 45, 255–262. 10.1016/j.molcel.2011.11.019. [PubMed: 22196887]
48. Xu J, Shao Z, Li D, Xie H, Kim W, Huang J, Taylor JE, Pinello L, Glass K, Jaffe JD, et al. (2015). Developmental control of polycomb subunit composition by GATA factors mediates a switch to non-canonical functions. Mol Cell 57, 304–316. 10.1016/j.molcel.2014.12.009. [PubMed: 25578878]

49. Ai S, Yu X, Li Y, Peng Y, Li C, Yue Y, Tao G, Li C, Pu WT, and He A (2017). Divergent Requirements for EZH1 in Heart Development Versus Regeneration. Circ Res 121, 106–112. 10.1161/CIRCRESAHA.117.311212. [PubMed: 28512107]
50. Bodega B, Marasca F, Ranzani V, Cherubini A, Della Valle F, Neguembor MV, Wassef M, Zippo A, Lanzuolo C, Pagani M, and Orlando V (2017). A cytosolic Ezh1 isoform modulates a PRC2-Ezh1 epigenetic adaptive response in postmitotic cells. Nat Struct Mol Biol 24, 444–452. 10.1038/nsmb.3392. [PubMed: 28346433]
51. Chen J, Liang X, Zhang S, Wang S, Garcia SP, Yan P, Yu H, Li Z, Liu L, Zhang F, et al. (2020). Two faces of bivalent domain regulate VEGFA responsiveness and angiogenesis. Cell Death Dis 11, 75. 10.1038/s41419-020-2228-3. [PubMed: 32001672]
52. Utsunomiya S, Kishi Y, Tsuboi M, Kawaguchi D, Gotoh Y, Abe M, Sakimura K, Maeda K, and Takemoto H (2021). Ezh1 regulates expression of Cpg15/Neuritin in mouse cortical neurons. Drug Discov Ther 15, 55–65. 10.5582/ddt.2021.01017. [PubMed: 33678755]
53. El Said NH, Della Valle F, Liu P, Paytuvi-Gallart A, Adroub S, Gimenez J, and Orlando V (2021). Malat-1-PRC2-EZH1 interaction supports adaptive oxidative stress dependent epigenome remodeling in skeletal myotubes. Cell Death Dis 12, 850. 10.1038/s41419-021-04082-z. [PubMed: 34531374]
54. Ryall JG, Dell'Orso S, Derfoul A, Juan A, Zare H, Feng X, Clermont D, Koulnis M, Gutierrez-Cruz G, Fulco M, and Sartorelli V (2015). The NAD(+)-dependent SIRT1 deacetylase translates a metabolic switch into regulatory epigenetics in skeletal muscle stem cells. Cell Stem Cell 16, 171–183. 10.1016/j.stem.2014.12.004. [PubMed: 25600643]
55. Dell'Orso S, Juan AH, Ko KD, Naz F, Perovanovic J, Gutierrez-Cruz G, Feng X, and Sartorelli V (2019). Single cell analysis of adult mouse skeletal muscle stem cells in homeostatic and regenerative conditions. Development 146. 10.1242/dev.174177.
56. Shcherbina A, Larouche J, Fraczek P, Yang BA, Brown LA, Markworth JF, Chung CH, Khaliq M, de Silva K, Choi JJ, et al. (2020). Dissecting Murine Muscle Stem Cell Aging through Regeneration Using Integrative Genomic Analysis. Cell Rep 32, 107964. 10.1016/j.celrep.2020.107964. [PubMed: 32726628]
57. Chakkalakal JV, Jones KM, Basson MA, and Brack AS (2012). The aged niche disrupts muscle stem cell quiescence. Nature 490, 355–360. 10.1038/nature11438. [PubMed: 23023126]
58. Garcia-Prat L, Perdiguero E, Alonso-Martin S, Dell'Orso S, Ravichandran S, Brooks SR, Juan AH, Campanario S, Jiang K, Hong X, et al. (2020). FoxO maintains a genuine muscle stem-cell quiescent state until geriatric age. Nat Cell Biol 22, 1307–1318. 10.1038/s41556-020-00593-7. [PubMed: 33106654]
59. Liu L, Cheung TH, Charville GW, Hurgo BM, Leavitt T, Shih J, Brunet A, and Rando TA (2013). Chromatin modifications as determinants of muscle stem cell quiescence and chronological aging. Cell Rep 4, 189–204. 10.1016/j.celrep.2013.05.043. [PubMed: 23810552]
60. Machado L, Esteves de Lima J, Fabre O, Proux C, Legendre R, Szegedi A, Varet H, Ingerslev LR, Barres R, Relaix F, and Mourikis P (2017). In Situ Fixation Redefines Quiescence and Early Activation of Skeletal Muscle Stem Cells. Cell Rep 21, 1982–1993. 10.1016/j.celrep.2017.10.080. [PubMed: 29141227]
61. van Velthoven CTJ, de Morree A, Egner IM, Brett JO, and Rando TA (2017). Transcriptional Profiling of Quiescent Muscle Stem Cells In Vivo. Cell Rep 21, 1994–2004. 10.1016/j.celrep.2017.10.037. [PubMed: 29141228]
62. Yablonka-Reuveni Z, Rudnicki MA, Rivera AJ, Primig M, Anderson JE, and Natanson P (1999). The transition from proliferation to differentiation is delayed in satellite cells from mice lacking MyoD. Dev Biol 210, 440–455. 10.1006/dbio.1999.9284. [PubMed: 10357902]
63. Sheehan SM, and Allen RE (1999). Skeletal muscle satellite cell proliferation in response to members of the fibroblast growth factor family and hepatocyte growth factor. J Cell Physiol 181, 499–506. 10.1002/(SICI)1097-4652(199912)181:3<499::AID-JCP14>3.0.CO;2-1. [PubMed: 10528236]
64. Jones NC, Fedorov YV, Rosenthal RS, and Olwin BB (2001). ERK1/2 is required for myoblast proliferation but is dispensable for muscle gene expression and cell fusion. J Cell Physiol 186, 104–115. 10.1002/1097-4652(200101)186:1<104::AID-JCP1015>3.0.CO;2-0. [PubMed: 11147804]

65. Pallafacchina G, Francois S, Regnault B, Czarny B, Dive V, Cumano A, Montarras D, and Buckingham M (2010). An adult tissue-specific stem cell in its niche: a gene profiling analysis of in vivo quiescent and activated muscle satellite cells. Stem Cell Res 4, 77–91. 10.1016/j.scr.2009.10.003. [PubMed: 19962952]
66. Hartl FU, Bracher A, and Hayer-Hartl M (2011). Molecular chaperones in protein folding and proteostasis. Nature 475, 324–332. 10.1038/nature10317. [PubMed: 21776078]
67. Garcia-Prat L, Sousa-Victor P, and Munoz-Canoves P (2017). Proteostatic and Metabolic Control of Stemness. Cell Stem Cell 20, 593–608. 10.1016/j.stem.2017.04.011. [PubMed: 28475885]
68. Vahidi Ferdousi L, Rocheteau P, Chayot R, Montagne B, Chaker Z, Flamant P, Tajbakhsh S, and Ricchetti M (2014). More efficient repair of DNA double-strand breaks in skeletal muscle stem cells compared to their committed progeny. Stem Cell Res 13, 492–507. 10.1016/j.scr.2014.08.005. [PubMed: 25262445]
69. Vasyutina E, Lenhard DC, Wende H, Erdmann B, Epstein JA, and Birchmeier C (2007). RBP-J (Rbpsuh) is essential to maintain muscle progenitor cells and to generate satellite cells. Proceedings of the National Academy of Sciences of the United States of America 104, 4443–4448. 10.1073/pnas.0610647104. [PubMed: 17360543]
70. Mourikis P, Sambasivan R, Castel D, Rocheteau P, Bizzarro V, and Tajbakhsh S (2012). A critical requirement for notch signaling in maintenance of the quiescent skeletal muscle stem cell state. Stem Cells 30, 243–252. 10.1002/stem.775. [PubMed: 22069237]
71. Bjornson CR, Cheung TH, Liu L, Tripathi PV, Steeper KM, and Rando TA (2012). Notch signaling is necessary to maintain quiescence in adult muscle stem cells. Stem Cells 30, 232–242. 10.1002/stem.773. [PubMed: 22045613]
72. Brohl D, Vasyutina E, Czajkowski MT, Griger J, Rassek C, Rahn HP, Purfurst B, Wende H, and Birchmeier C (2012). Colonization of the satellite cell niche by skeletal muscle progenitor cells depends on Notch signals. Developmental cell 23, 469–481. 10.1016/j.devcel.2012.07.014. [PubMed: 22940113]
73. Castel D, Mourikis P, Bartels SJ, Brinkman AB, Tajbakhsh S, and Stunnenberg HG (2013). Dynamic binding of RBPJ is determined by Notch signaling status. Genes Dev 27, 1059–1071. 10.1101/gad.211912.112. [PubMed: 23651858]
74. Seale P, Sabourin LA, Girgis-Gabardo A, Mansouri A, Gruss P, and Rudnicki MA (2000). Pax7 is required for the specification of myogenic satellite cells. Cell 102, 777–786. [PubMed: 11030621]
75. Wen Y, Bi P, Liu W, Asakura A, Keller C, and Kuang S (2012). Constitutive Notch activation upregulates Pax7 and promotes the self-renewal of skeletal muscle satellite cells. Mol Cell Biol 32, 2300–2311. 10.1128/MCB.06753-11. [PubMed: 22493066]
76. Shea KL, Xiang W, LaPorta VS, Licht JD, Keller C, Basson MA, and Brack AS (2010). Sprouty1 regulates reversible quiescence of a self-renewing adult muscle stem cell pool during regeneration. Cell stem cell 6, 117–129. 10.1016/j.stem.2009.12.015. [PubMed: 20144785]
77. Zhou Y, Cheunsuchon P, Nakayama Y, Lawlor MW, Zhong Y, Rice KA, Zhang L, Zhang X, Gordon FE, Lidov HG, et al. (2010). Activation of paternally expressed genes and perinatal death caused by deletion of the Gtl2 gene. Development 137, 2643–2652. 10.1242/dev.045724. [PubMed: 20610486]
78. Fukada S, Uezumi A, Ikemoto M, Masuda S, Segawa M, Tanimura N, Yamamoto H, Miyagoe-Suzuki Y, and Takeda S (2007). Molecular signature of quiescent satellite cells in adult skeletal muscle. Stem Cells 25, 2448–2459. 10.1634/stemcells.2007-0019. [PubMed: 17600112]
79. Zammit PS, Heslop L, Hudon V, Rosenblatt JD, Tajbakhsh S, Buckingham ME, Beauchamp JR, and Partridge TA (2002). Kinetics of myoblast proliferation show that resident satellite cells are competent to fully regenerate skeletal muscle fibers. Exp Cell Res 281, 39–49. [PubMed: 12441128]
80. Tang AH, and Rando TA (2014). Induction of autophagy supports the bioenergetic demands of quiescent muscle stem cell activation. EMBO J 33, 2782–2797. 10.15252/embj.201488278. [PubMed: 25316028]
81. Murphy MM, Lawson JA, Mathew SJ, Hutcheson DA, and Kardon G (2011). Satellite cells, connective tissue fibroblasts and their interactions are crucial for muscle regeneration. Development 138, 3625–3637. 10.1242/dev.064162. [PubMed: 21828091]

82. Mo A, Mukamel EA, Davis FP, Luo C, Henry GL, Picard S, Urich MA, Nery JR, Sejnowski TJ, Lister R, et al. (2015). Epigenomic Signatures of Neuronal Diversity in the Mammalian Brain. Neuron 86, 1369–1384. 10.1016/j.neuron.2015.05.018. [PubMed: 26087164]
83. Grau D, Zhang Y, Lee CH, Valencia-Sanchez M, Zhang J, Wang M, Holder M, Svetlov V, Tan D, Nudler E, et al. (2021). Structures of monomeric and dimeric PRC2:EZH1 reveal flexible modules involved in chromatin compaction. Nat Commun 12, 714. 10.1038/s41467-020-20775-z. [PubMed: 33514705]
84. Mauro A (1961). Satellite cell of skeletal muscle fibers. J Biophys Biochem Cytol 9, 493–495. 10.1083/jcb.9.2.493. [PubMed: 13768451]
85. Dong A, Liu J, Lin K, Zeng W, So WK, Hu S, and Cheung TH (2022). Global chromatin accessibility profiling analysis reveals a chronic activation state in aged muscle stem cells. iScience 25, 104954. 10.1016/j.isci.2022.104954. [PubMed: 36093058]
86. Vo LT, Kinney MA, Liu X, Zhang Y, Barragan J, Sousa PM, Jha DK, Han A, Cesana M, Shao Z, et al. (2018). Regulation of embryonic haematopoietic multipotency by EZH1. Nature 553, 506–510. 10.1038/nature25435. [PubMed: 29342143]
87. Wosczyna MN, and Rando TA (2018). A Muscle Stem Cell Support Group: Coordinated Cellular Responses in Muscle Regeneration. Dev Cell 46, 135–143. 10.1016/j.devcel.2018.06.018. [PubMed: 30016618]
88. Cutler AA, Pawlikowski B, Wheeler JR, Dalla Betta N, Elston T, O'Rourke R, Jones K, and Olwin BB (2022). The regenerating skeletal muscle niche drives satellite cell return to quiescence. iScience 25, 104444. 10.1016/j.isci.2022.104444. [PubMed: 35733848]
89. Aran D, Looney AP, Liu L, Wu E, Fong V, Hsu A, Chak S, Naikawadi RP, Wolters PJ, Abate AR, et al. (2019). Reference-based analysis of lung single-cell sequencing reveals a transitional profibrotic macrophage. Nat Immunol 20, 163–172. 10.1038/s41590-018-0276-y. [PubMed: 30643263]
90. Mann CJ, Perdiguero E, Kharraz Y, Aguilar S, Pessina P, Serrano AL, and Munoz-Canoves P (2011). Aberrant repair and fibrosis development in skeletal muscle. Skelet Muscle 1, 21. 10.1186/2044-5040-1-21. [PubMed: 21798099]
91. Maier MM, and Gessler M (2000). Comparative analysis of the human and mouse Hey1 promoter: Hey genes are new Notch target genes. Biochem Biophys Res Commun 275, 652–660. 10.1006/bbrc.2000.3354. [PubMed: 10964718]
92. Yatim A, Benne C, Sobhian B, Laurent-Chabalier S, Deas O, Judde JG, Lelievre JD, Levy Y, and Benkirane M (2012). NOTCH1 nuclear interactome reveals key regulators of its transcriptional activity and oncogenic function. Mol Cell 48, 445–458. 10.1016/j.molcel.2012.08.022. [PubMed: 23022380]
93. Fu W, Asp P, Canter B, and Dynlacht BD (2014). Primary cilia control hedgehog signaling during muscle differentiation and are deregulated in rhabdomyosarcoma. Proc Natl Acad Sci U S A 111, 9151–9156. 10.1073/pnas.1323265111. [PubMed: 24927541]
94. Jaafar Marican NH, Cruz-Migoni SB, and Borycki AG (2016). Asymmetric Distribution of Primary Cilia Allocates Satellite Cells for Self-Renewal. Stem Cell Reports 6, 798–805. 10.1016/j.stemcr.2016.04.004. [PubMed: 27161363]
95. Goto H, Inaba H, and Inagaki M (2017). Mechanisms of ciliogenesis suppression in dividing cells. Cell Mol Life Sci 74, 881–890. 10.1007/s00018-016-2369-9. [PubMed: 27669693]
96. Palla AR, Hilgendorf KI, Yang AV, Kerr JP, Hinken AC, Demeter J, Kraft P, Mooney NA, Yucel N, Burns DM, et al. (2022). Primary cilia on muscle stem cells are critical to maintain regenerative capacity and are lost during aging. Nat Commun 13, 1439. 10.1038/s41467-022-29150-6. [PubMed: 35301320]
97. Brun CE, Sincennes MC, Lin AYT, Hall D, Jarassier W, Feige P, Le Grand F, and Rudnicki MA (2022). GLI3 regulates muscle stem cell entry into GAlert and self-renewal. Nat Commun 13, 3961. 10.1038/s41467-022-31695-5. [PubMed: 35803939]
98. Goetz SC, and Anderson KV (2010). The primary cilium: a signalling centre during vertebrate development. Nat Rev Genet 11, 331–344. 10.1038/nrg2774. [PubMed: 20395968]
99. Wheway G, Nazlamova L, and Hancock JT (2018). Signaling through the Primary Cilium. Front Cell Dev Biol 6, 8. 10.3389/fcell.2018.00008. [PubMed: 29473038]

100. Chen JK, Taipale J, Young KE, Maiti T, and Beachy PA (2002). Small molecule modulation of Smoothened activity. Proc Natl Acad Sci U S A 99, 14071–14076. 10.1073/pnas.182542899. [PubMed: 12391318]

101. Struhl G, Fitzgerald K, and Greenwald I (1993). Intrinsic activity of the Lin-12 and Notch intracellular domains in vivo. Cell 74, 331–345. 10.1016/0092-8674(93)90424-o. [PubMed: 8343960]

102. Schroeter EH, Kisslinger JA, and Kopan R (1998). Notch-1 signalling requires ligand-induced proteolytic release of intracellular domain. Nature 393, 382–386. 10.1038/30756. [PubMed: 9620803]

103. Kopan R, and Ilagan MX (2009). The canonical Notch signaling pathway: unfolding the activation mechanism. Cell 137, 216–233. 10.1016/j.cell.2009.03.045. [PubMed: 19379690]

104. Jiao L, Shubbar M, Yang X, Zhang Q, Chen S, Wu Q, Chen Z, Rizo J, and Liu X (2020). A partially disordered region connects gene repression and activation functions of EZH2. Proc Natl Acad Sci U S A 117, 16992–17002. 10.1073/pnas.1914866117. [PubMed: 32631994]

105. Pasut A, Chang NC, Gurriaran-Rodriguez U, Faulkes S, Yin H, Lacaria M, Ming H, and Rudnicki MA (2016). Notch Signaling Rescues Loss of Satellite Cells Lacking Pax7 and Promotes Brown Adipogenic Differentiation. Cell Rep 16, 333–343. 10.1016/j.celrep.2016.06.001. [PubMed: 27346341]

106. Marescal O, and Cheeseman IM (2020). Cellular Mechanisms and Regulation of Quiescence. Dev Cell 55, 259–271. 10.1016/j.devcel.2020.09.029. [PubMed: 33171109]

107. Haller S, Kapuria S, Riley RR, O'Leary MN, Schreiber KH, Andersen JK, Melov S, Que J, Rando TA, Rock J, et al. (2017). mTORC1 Activation during Repeated Regeneration Impairs Somatic Stem Cell Maintenance. Cell Stem Cell 21, 806–818 e805. 10.1016/j.stem.2017.11.008. [PubMed: 29220665]

108. Baghdadi MB, Castel D, Machado L, Fukada SI, Birk DE, Relaix F, Tajbakhsh S, and Mourikis P (2018). Reciprocal signalling by Notch-Collagen V-CALCR retains muscle stem cells in their niche. Nature 557, 714–718. 10.1038/s41586-018-0144-9. [PubMed: 29795344]

109. Verdijk LB, Koopman R, Schaart G, Meijer K, Savelberg HH, and van Loon LJ (2007). Satellite cell content is specifically reduced in type II skeletal muscle fibers in the elderly. Am J Physiol Endocrinol Metab 292, E151–157. 10.1152/ajpendo.00278.2006. [PubMed: 16926381]

110. Fujita R, and Crist C (2018). Translational Control of the Myogenic Program in Developing, Regenerating, and Diseased Skeletal Muscle. Curr Top Dev Biol 126, 67–98. 10.1016/bs.ctdb.2017.08.004. [PubMed: 29305004]

111. Baker N, Wade S, Triolo M, Girgis J, Chwastek D, Larrigan S, Feige P, Fujita R, Crist C, Rudnicki MA, et al. (2022). The mitochondrial protein OPA1 regulates the quiescent state of adult muscle stem cells. Cell Stem Cell 29, 1315–1332 e1319. 10.1016/j.stem.2022.07.010. [PubMed: 35998642]

112. Hong X, Isern J, Campanario S, Perdiguero E, Ramirez-Pardo I, Segales J, Hernansanz-Agustin P, Curtabbi A, Deryagin O, Pollan A, et al. (2022). Mitochondrial dynamics maintain muscle stem cell regenerative competence throughout adult life by regulating metabolism and mitophagy. Cell Stem Cell 29, 1506–1508. 10.1016/j.stem.2022.09.002. [PubMed: 36206734]

113. Vizan P, Gutierrez A, Espejo I, Garcia-Montolio M, Lange M, Carretero A, Lafzi A, de Andres-Aguayo L, Blanco E, Thambyrajah R, et al. (2020). The Polycomb-associated factor PHF19 controls hematopoietic stem cell state and differentiation. Sci Adv 6, eabb2745. 10.1126/sciadv.abb2745. [PubMed: 32821835]

114. Hidalgo I, Herrera-Merchan A, Ligos JM, Carramolino L, Nunez J, Martinez F, Dominguez O, Torres M, and Gonzalez S (2012). Ezh1 is required for hematopoietic stem cell maintenance and prevents senescence-like cell cycle arrest. Cell Stem Cell 11, 649–662. 10.1016/j.stem.2012.08.001. [PubMed: 23122289]

115. Jing R, Scarfo I, Najia MA, Lummertz da Rocha E, Han A, Sanborn M, Bingham T, Kubaczka C, Jha DK, Falchetti M, et al. (2022). EZH1 repression generates mature iPSC-derived CAR T cells with enhanced antitumor activity. Cell Stem Cell 29, 1181–1196 e1186. 10.1016/j.stem.2022.06.014. [PubMed: 35931029]

116. van Mierlo G, Veenstra GJC, Vermeulen M, and Marks H (2019). The Complexity of PRC2 Subcomplexes. Trends Cell Biol 29, 660–671. 10.1016/j.tcb.2019.05.004. [PubMed: 31178244]
117. Kuang S, Charge SB, Seale P, Huh M, and Rudnicki MA (2006). Distinct roles for Pax7 and Pax3 in adult regenerative myogenesis. J Cell Biol 172, 103–113. 10.1083/jcb.200508001. [PubMed: 16391000]
118. von Maltzahn J, Jones AE, Parks RJ, and Rudnicki MA (2013). Pax7 is critical for the normal function of satellite cells in adult skeletal muscle. Proc Natl Acad Sci U S A 110, 16474–16479. 10.1073/pnas.1307680110. [PubMed: 24065826]
119. Conboy IM, Conboy MJ, Smythe GM, and Rando TA (2003). Notch-mediated restoration of regenerative potential to aged muscle. Science 302, 1575–1577. 10.1126/science.1087573. [PubMed: 14645852]
120. Ezratty EJ, Stokes N, Chai S, Shah AS, Williams SE, and Fuchs E (2011). A role for the primary cilium in Notch signaling and epidermal differentiation during skin development. Cell 145, 1129–1141. 10.1016/j.cell.2011.05.030. [PubMed: 21703454]
121. Soto RA, Najia MAT, Hachimi M, Frame JM, Yette GA, Lummertz da Rocha E, Stankunas K, Daley GQ, and North TE (2021). Sequential regulation of hemogenic fate and hematopoietic stem and progenitor cell formation from arterial endothelium by Ezh1/2. Stem Cell Reports 16, 1718–1734. 10.1016/j.stemcr.2021.05.014. [PubMed: 34143974]
122. MacDonald HR, and Zaech P (1982). Light scatter analysis and sorting of cells activated in mixed leukocyte culture. Cytometry 3, 55–58. 10.1002/cyto.990030112. [PubMed: 6214385]
123. Liu L, Cheung TH, Charville GW, and Rando TA (2015). Isolation of skeletal muscle stem cells by fluorescence-activated cell sorting. Nat Protoc 10, 1612–1624. 10.1038/nprot.2015.110. [PubMed: 26401916]
124. Riparini G, Simone JM, and Sartorelli V (2022). FACS-isolation and Culture of Fibro-Adipogenic Progenitors and Muscle Stem Cells from Unperturbed and Injured Mouse Skeletal Muscle. J Vis Exp. 10.3791/63983.
125. Feng X, Naz F, Juan AH, Dell'Orso S, and Sartorelli V (2018). Identification of Skeletal Muscle Satellite Cells by Immunofluorescence with Pax7 and Laminin Antibodies. J Vis Exp. 10.3791/57212.
126. Hsieh JJ, Henkel T, Salmon P, Robey E, Peterson MG, and Hayward SD (1996). Truncated mammalian Notch1 activates CBF1/RBPJk-repressed genes by a mechanism resembling that of Epstein-Barr virus EBNA2. Mol Cell Biol 16, 952–959. 10.1128/MCB.16.3.952. [PubMed: 8622698]
127. Trapnell C, Pachter L, and Salzberg SL (2009). TopHat: discovering splice junctions with RNA-Seq. Bioinformatics 25, 1105–1111. [PubMed: 19289445]
128. Butler A, Hoffman P, Smibert P, Papalexi E, and Satija R (2018). Integrating single-cell transcriptomic data across different conditions, technologies, and species. Nat Biotechnol 36, 411–420. 10.1038/nbt.4096. [PubMed: 29608179]
129. Stuart T, Butler A, Hoffman P, Hafemeister C, Papalexi E, Mauck WM 3rd, Hao Y, Stoeckius M, Smibert P, and Satija R (2019). Comprehensive Integration of Single-Cell Data. Cell 177, 1888–1902 e1821. 10.1016/j.cell.2019.05.031. [PubMed: 31178118]
130. Qiu X, Mao Q, Tang Y, Wang L, Chawla R, Pliner HA, and Trapnell C (2017). Reversed graph embedding resolves complex single-cell trajectories. Nat Methods 14, 979–982. 10.1038/nmeth.4402. [PubMed: 28825705]
131. Trapnell C, Cacchiarelli D, Grimsby J, Pokharel P, Li S, Morse M, Lennon NJ, Livak KJ, Mikkelsen TS, and Rinn JL (2014). The dynamics and regulators of cell fate decisions are revealed by pseudotemporal ordering of single cells. Nat Biotechnol 32, 381–386. 10.1038/nbt.2859. [PubMed: 24658644]
132. Cao J, Spielmann M, Qiu X, Huang X, Ibrahim DM, Hill AJ, Zhang F, Mundlos S, Christiansen L, Steemers FJ, et al. (2019). The single-cell transcriptional landscape of mammalian organogenesis. Nature. 10.1038/s41586-019-0969-x.
133. Langmead B, Trapnell C, Pop M, and Salzberg SL (2009). Ultrafast and memory-efficient alignment of short DNA sequences to the human genome. Genome Biol 10, R25. 10.1186/gb-2009-10-3-r25. [PubMed: 19261174]

134. Zhang Y, Liu T, Meyer CA, Eeckhoute J, Johnson DS, Bernstein BE, Nussbaum C, Myers RM, Brown M, Li W, and Liu XS (2008). Model-based analysis of ChIP-Seq (MACS). Genome Biol 9, R137. [PubMed: 18798982]

135. Kent WJ, Zweig AS, Barber G, Hinrichs AS, and Karolchik D (2010). BigWig and BigBed: enabling browsing of large distributed datasets. Bioinformatics 26, 2204–2207. 10.1093/bioinformatics/btq351. [PubMed: 20639541]

136. Quinlan AR, and Hall IM (2010). BEDTools: a flexible suite of utilities for comparing genomic features. Bioinformatics 26, 841–842. 10.1093/bioinformatics/btq033. [PubMed: 20110278]

137. Xu HB, Luo X, Qian J, Pang XH, Song JY, Qian GR, Chen JH, and Chen SL (2012). FastUniq: A Fast De Novo Duplicates Removal Tool for Paired Short Reads. Plos One 7. ARTN e52249 10.1371/journal.pone.0052249.

Highlights

- Ezh1 is required to maintain quiescence of muscle stem cells (MuSCs)
- Ezh1-null mice display muscle regenerative defects
- Ezh1 regulates the Notch pathway
- Genetic reconstitution of Notch pathway corrects premature activation of $Ezh1^{-/-}$ MuSCs

A

Up-regulated genes in *Ezh1*$^{-/-}$ FI MuSCs

Enriched terms	Count	Log P-Value
Metabolism of RNA	34	-10.21236
Ribonucleoprotein complex biogenesis	28	-8.7218643913
Transmembrane receptor protein tyrosine kinase signaling pathway	31	-7.824059968
Negative regulation of cellular component movement	22	-7.5615394698
ERK1 and ERK2 cascade	22	-7.42037175

B

Down-regulated genes in *Ezh1*$^{-/-}$ FI MuSCs

Enriched terms	Count	Log P-Value
Protein folding	16	-7.7630894304
Cellular response to DNA damage stimulus	35	-6.4021004362
Regulation of mitotic cell cycle	26	-5.1092802528
DNA replication	16	-5.013057754
Skeletal muscle tissue development	14	-4.7783576209

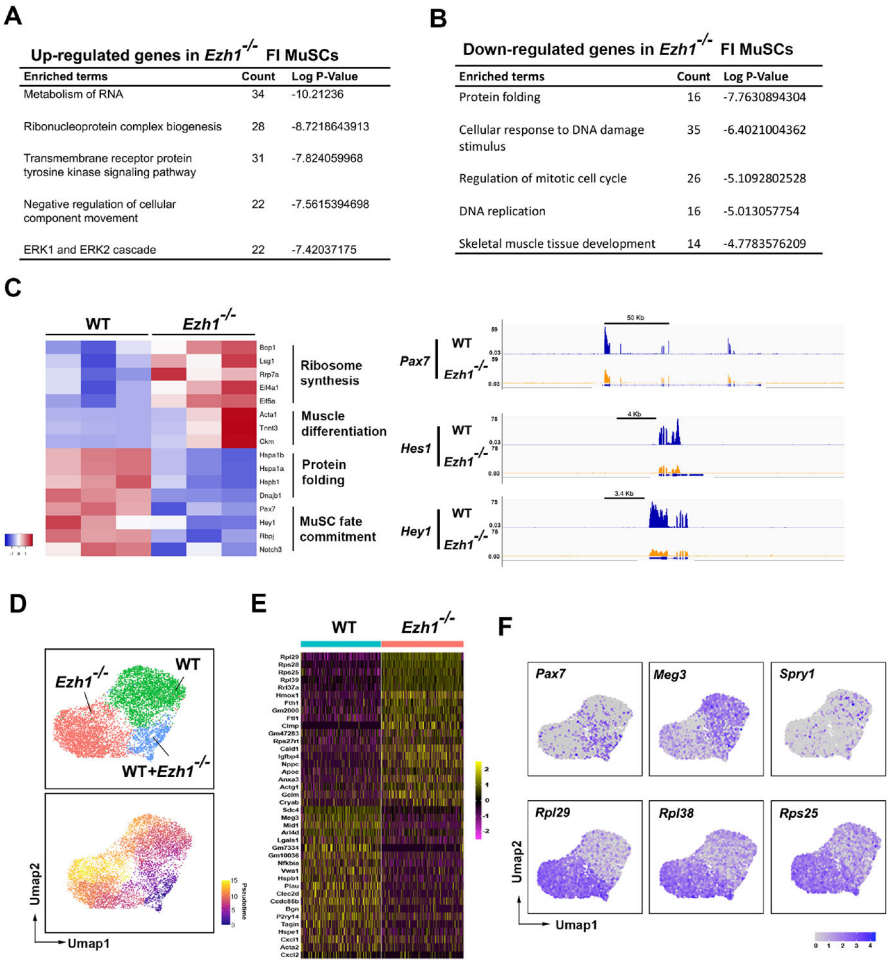

Figure 1. Transcriptomes of wild-type and *Ezh1*$^{-/-}$ FACS-isolated MuSCs

(A) List of up-regulated and (B) downregulated GO terms in *Ezh1*$^{-/-}$ MuSCs. (C) Heatmap of transcripts differentially expressed (left panel) and RNA-seq tracks of the indicated transcripts in WT and *Ezh1*$^{-/-}$ MuSCs (right panel). (D) scRNA-seq UMAP plot of WT and *Ezh1*$^{-/-}$ clusters (top panel) and heatmap-based pseudotime ordering (bottom panel). (E) scRNA-seq heatmap of differentially expressed genes in WT and *Ezh1*$^{-/-}$ MuSCs. (F) Feature plots of the indicated transcripts in UMAP clusters represented in (D). See also Figure S1 and Table S1

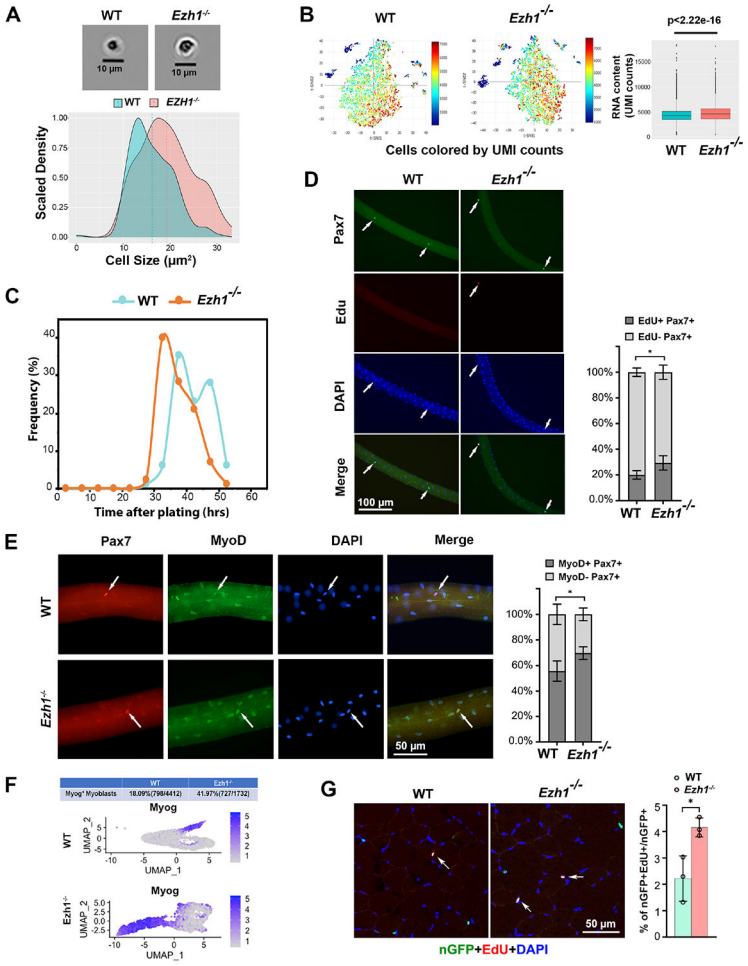

Figure 2. *Ezh1*$^{-/-}$ MuSCs are constitutively activated

(A) Images of WT and *Ezh1*$^{-/-}$ MuSCs obtained from littermate mice immediately after FACS isolation (top panel) and cell size quantification determined by FACS forward scatter intensity (bottom panel). (B) UMI counts (left panel) and RNA content quantification (right panel) of WT and *Ezh1*$^{-/-}$ MuSCs. (C) WT and *Ezh1*$^{-/-}$ MuSCs undergoing first cell division determined by time lapse microscopy. (D) Pax7 immunofluorescent staining and Edu incorporation of myofiber-associated WT and *Ezh1*$^{-/-}$ MuSCs cultured for 28 hr after dissociation. DAPI identifies cell nuclei. Quantification of Pax7^{+}/EdU^{+} and Pax7^{+}/EdU^{-} MuSCs. Data are represented as mean ± SD (60 single myofibers from 4 mice), *p-value <0.05. (E) Pax7 and MyoD immunofluorescence staining of myofiber-associated MuSCs cultured for 24 hr after dissociation. Quantification of Pax7^{+}/MyoD^{+} and Pax7^{+}/MyoD^{-} MuSCs. Data are represented as mean ± SD (60 single myofibers from 4 mice), *p-value <0.05. (F) scRNA-seq UMAP for Myogenin in WT and *Ezh1*$^{-/-}$ primary myoblasts. 18% of WT primary myoblasts express Myogenin compared to 41.9% of *Ezh1*$^{-/-}$ primary myoblasts. (G). Muscle sections of Pax7^{CreERT2}; *ROSA26*$^{STOP\text{-}Sun1\text{-}GFP}$(WT) *or* Pax7^{CreERT2}; *ROSA26*$^{STOP\text{-}Sun1\text{-}GFP}$; *Ezh1*$^{-/-}$ (*Ezh1*$^{-/-}$) mice intraperitoneally injected with tamoxifen and EdU (see Experimental Procedures). Quantification of nGFP^{+}-Edu^{+} MuSCs/ total nGFP^{+} cells in WT and *Ezh1*$^{-/-}$ mice. Data are represented as mean ± SD (n=3 mice), *p-value <0.05. See also Figure S2 and Table S2

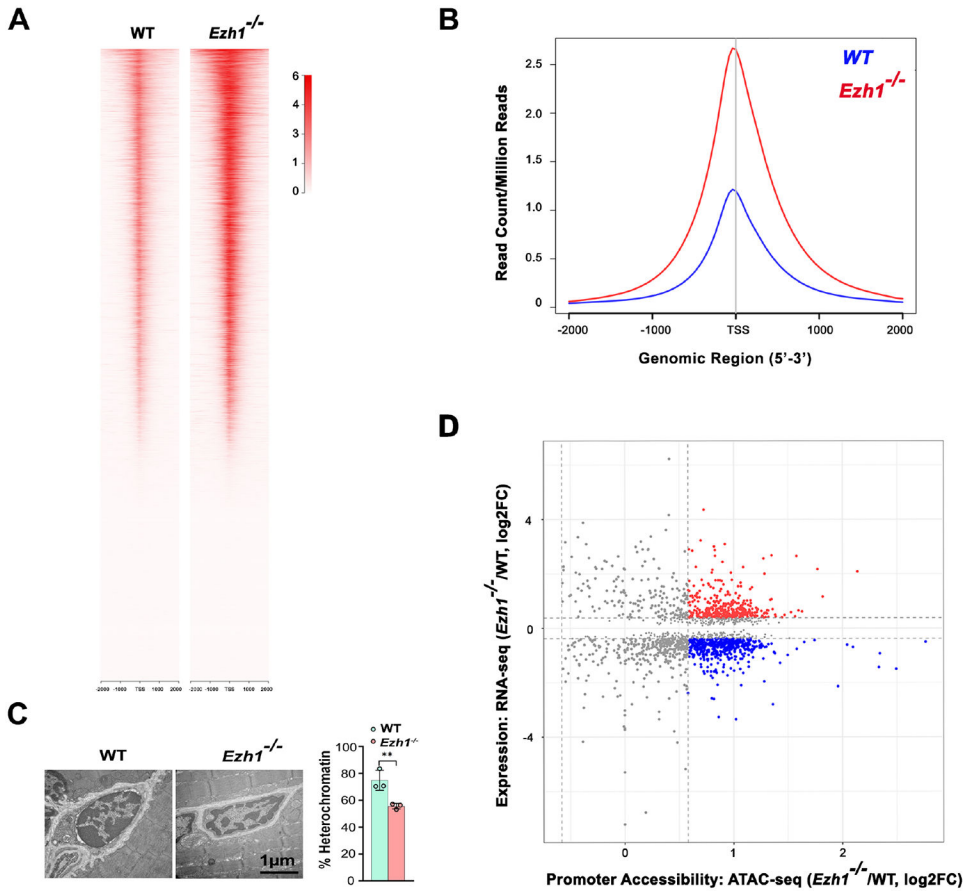

Figure 3. Ezh1 compacts MuSC chromatin

(A) ATAC-seq heatmaps of WT or *Ezh1*$^{-/-}$ MuSCs obtained from littermate mice. Signal (log_2) is centered −2Kb/+2Kb from the transcriptional start site (TSS). (B) Averaged ATAC-seq signal densities (read counts per million mapped reads, RPKM) in WT or *Ezh1*$^{-/-}$ MuSCs. (C) Representative transmission electron microscopy (TEM) images of muscle sections documenting reduced condensed heterochromatin in quiescent *Ezh1*$^{-/-}$ MuSCs (left panel). Scale bar represents 1 μm. Quantification of heterochromatin percentage in WT or *Ezh1*$^{-/-}$ MuSCs (right panel). Data are represented as mean ± SD (n=3), **p-value <0.01. (D) Integrated correlation plot of RNA-seq (y-axis) and promoter accessibility evaluated by ATAC-seq (x-axis) of *Ezh1*$^{-/-}$ /WT MuSCs values. Red dots correspond to genes with increased promoter chromatin accessibility and up-regulated transcripts in *Ezh1*$^{-/-}$ MuSCs. Blue dots correspond to genes with increased promoter chromatin accessibility and down-regulated transcripts in *Ezh1*$^{-/-}$ MuSCs. Expression is at least 1.3 fold-induction/reduction for up-regulated and down-regulated transcripts in *Ezh1*$^{-/-}$ MuSCs, respectively, with *p-value <0.05. Both up- and down-regulated genes display increased chromatin accessibility (1.5-fold, *p-value <0.05) in *Ezh1*$^{-/-}$ compared to WT MuSCs. See also Figure S3 and Table S3

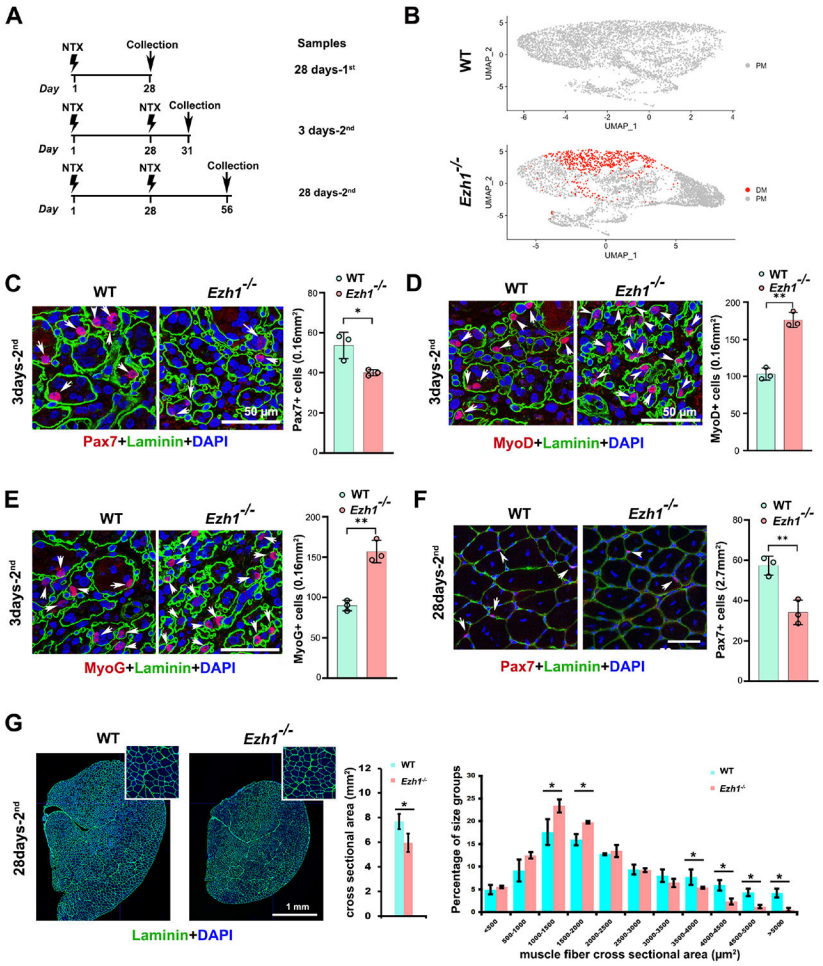

Figure 4. Muscle regeneration is impaired in the absence of Ezh1

(A) Scheme indicating muscle injury regimen. NTX, notexin. 28 days-1st are samples collected 28 days after first injury; 3 days- and 28 days-2nd are samples collected after 3 days or 28 days after second injury. (B) scRNA-seq UMAP of WT and *Ezh1*$^{-/-}$ MuSCs FACS- isolated 3 days post-2nd injury, PM (in grey) identifies cells with proliferating myoblast transcriptomes and DM (in red) cells with differentiating myocyte transcriptomes in the reference set [55]. (C) Pax7 and laminin immunostaining of muscle sections obtained 3 days-2nd injury of littermate WT or *Ezh1*$^{-/-}$ mice. DAPI indentifies cell nuclei. Quantification of Pax7^{+} cells in WT and *Ezh1*$^{-/-}$ muscle sections. Four (4) muscle sections from the same mouse were analyzed. Data are represented as mean ± SD (n=3 mice), *p-value <0.05. (D) MyoD and laminin immunostaining of muscle sections obtained 3 days-2nd injury of WT or *Ezh1*$^{-/-}$ mice. DAPI indentifies cell nuclei. Quantification of MyoD^{+} cells in WT and *Ezh1*$^{-/-}$ muscle sections. Four (4) muscle sections from the same mouse were analyzed. Data are represented as mean ± SD (n=3 mice), **p-value <0.01. (E) Myogenin and laminin immunostaining of muscle sections obtained 3 days-2nd injury of WT or *Ezh1*$^{-/-}$ mice. DAPI indentifies cell nuclei. Quantification of Myogenin^{+} cells in WT and *Ezh1*$^{-/-}$ muscle sections. Four (4) muscle sections from the same mouse were analyzed. Data are represented as mean ± SD (n=3 mice), **p-value <0.01. (F) Pax7 and laminin immunostaining of muscle sections obtained 28 days-2nd injury of WT or

Ezh1$^{-/-}$ mice. DAPI indentifies cell nuclei. Four (4) muscle sections from the same mouse were analyzed. Data are represented as mean ± SD (n=3 mice), **p-value <0.01. (G) Laminin staining of muscle sections obtained 28 days-2nd injury of WT or *Ezh1*$^{-/-}$ mice. Approximately 1,000-1,500 myofibers/mouse were quantified. Data are represented as mean ± SD (n=3 mice), *p-value <0.05. Muscle fiber cross sectional area (CSA) quantification and percentage of size gropus of WT or *Ezh1*$^{-/-}$ mice, *p-value <0.05. See also Figure S4, S5

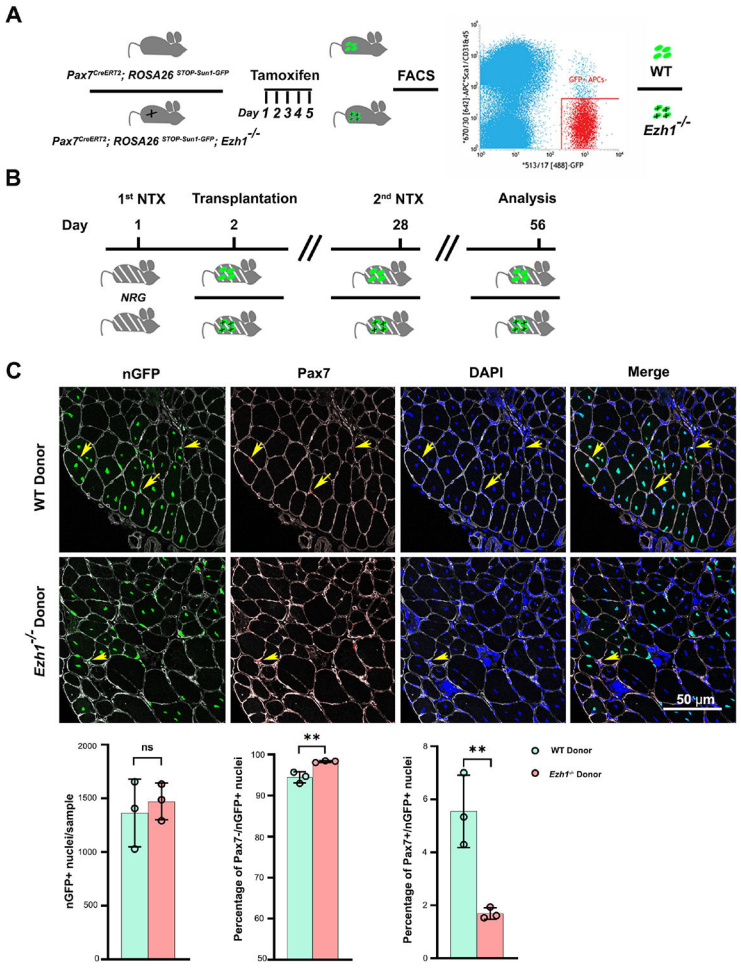

Figure 5. *Ezh1*$^{-/-}$ MuSCs fail to efficiently return to their niche

(A) Scheme of *Pax7*^{CreERT2}*; ROSA26*$^{STOP\text{-}Sun1\text{-}GFP}$ or *Pax7*^{CreERT2}*; ROSA26*$^{STOP\text{-}Sun1\text{-}GFP}$*; Ezh1*$^{-/-}$ mice tamoxifen treatment and representative FACS plot of nGFP^{+} cells isolation. (B) Scheme illustrating the transplantation protocol. (C) Nuclear GFP (nGFP) and Pax7 immunostating of muscle sections from immunodeficient NRG mice transplanted with either WT-nGFP or *Ezh1*$^{-/-}$-nGFP MuSCs (upper panel). Quantification of transplanted nGFP^{+} cells, percentages of Pax7^{-}/nGFP^{+}, and Pax7^{+}/nGFP^{+} cells from WT or *Ezh1*$^{-/-}$ in immunodeficient NRG muscle sections. Data are represented as mean ± SD (n=3 mice), ns (non significant); **p-value <0.01.

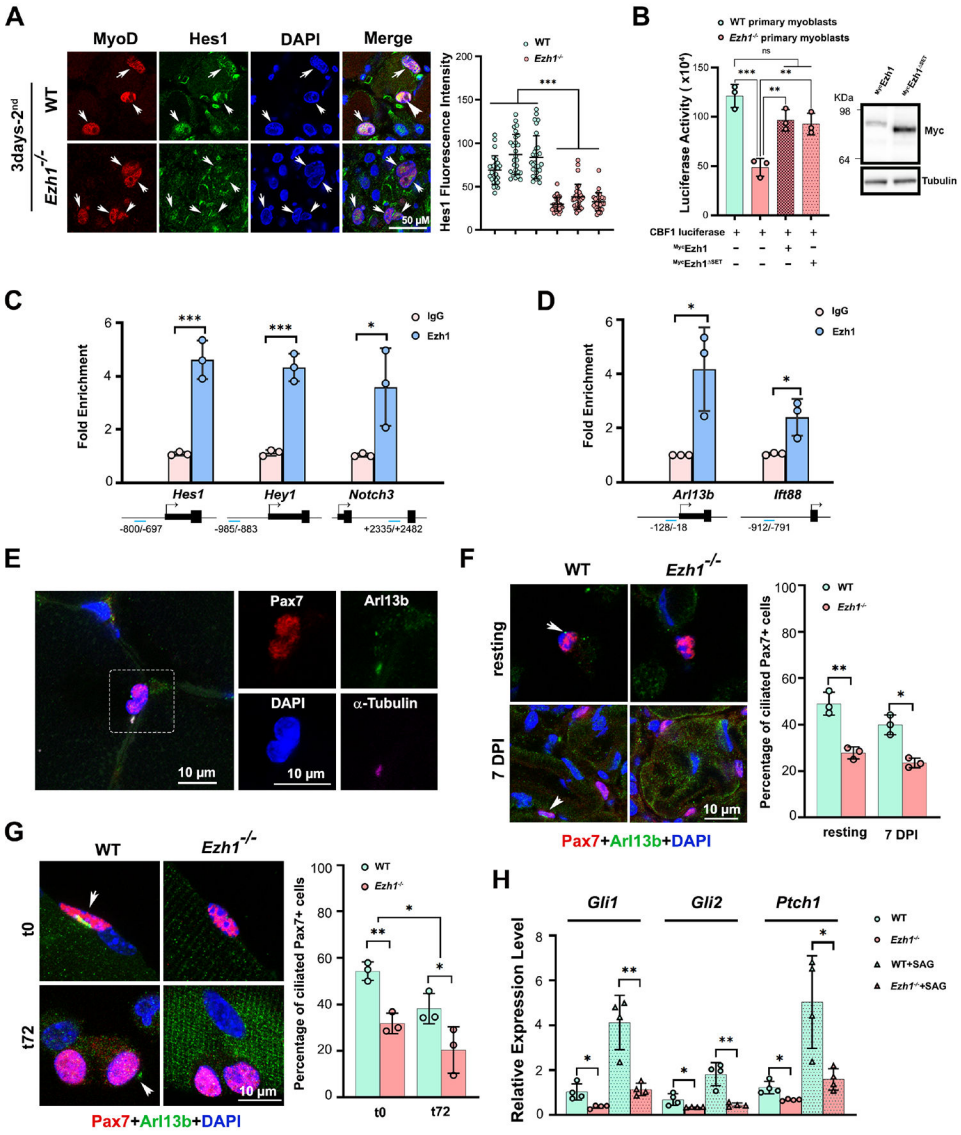

Figure 6. Ezh1 targets the Notch and cilium pathways

(A) MyoD and Hes1 immunostaining of muscle sections obtained 3 days-2nd injury of littermate WT or *Ezh1*$^{-/-}$ mice. DAPI indentifies cell nuclei (left panel).Quantification of Hes1 fluorescence signal in WT and *Ezh1*$^{-/-}$ muscle sections (right panel). Each dot represents fluorescent intensity of a single cell. Data are represented as mean SD (n=3 mice), ***p-value <0.001. (B) Relative luciferase activity of primary myoblasts isolated from either WT or *Ezh1*$^{-/-}$ mice and transfected with a Notch reporter construct (multimerized CBF1-luc). *Ezh1*$^{-/-}$ myoblasts were transfected with Myc-tagged full length Ezh1 or catalytic-inactive Myc-tagged Ezh1$^{\Delta SET}$ expression vector. Data are represented as mean ± SD (n=3),** p-value <0.01; *** <0.001, ns (non significant) (left panel). Immunoblot of cell extracts derived from *Ezh1*$^{-/-}$ myoblasts transfected with either Myc-tagged full length Ezh1 or catalytic-inactive Myc-tagged *Ezh1*$^{\Delta SET}$ expression vector probed with anti-Myc and anti-tubulin antibodies (right panel). (C) ChIP-qPCR assay with IgG or Ezh1 antibodies at Hes1, Hey1, and Notch3 regulatory regions performed on MuSC

chromatin. Location of the DNA primers employed is indicated in reference to the gene transcriptional start site (arrow). Data are represented as mean ± SD (n=3), ***p-value <0.001, *<0.05. (D) ChIP-qPCR assay with IgG or Ezh1 antibodies at Arl13b and ITF88 regulatory regions performed on on MuSC chromatin. Location of the DNA primers employed is indicated in reference to the gene transcriptional start site (arrow). Data are represented as mean ± SD (n=3), *p-value <0.05. (E) Immunostaining of TA muscle sections with Pax7, Arl13b and acetylated α-Tubulin antibodies. DAPI identifies cell nuclei. (F) Immunostaining of TA muscle sections obtained from either WT or *Ezh1*$^{-/-}$ mice in homeostatic (resting) conditions or 7 days afer NTX injury with Pax7, Arl13b antibodies. Quantification of ciliated (Pax7^{+}/Arl13^{+}) MuSCs. Data are represented as mean ± SD (n=3 mice), **p-value <0.01. (G) Immunostaining of myofibers isolated from either WT or *Ezh1*$^{-/-}$ mice immediately fixed (t0) or cultured for 72 hr (t72) with Pax7 and Arl13b antibodies. Quantification of ciliated (Pax7^{+}/Arl13^{+}) MuSCs. Data are represented as mean ± SD (n=3), ** p-value <0.01, * <0.05. (H) Relative expression of Gli1, Gli2, and Ptch1 evaluated by quantitative PCR in WT or *Ezh1*$^{-/-}$ MuSCs treated with DMSO or SAG1.3. Data are represented as mean ± SD (n=3), **p-value <0.01, * <0.05.

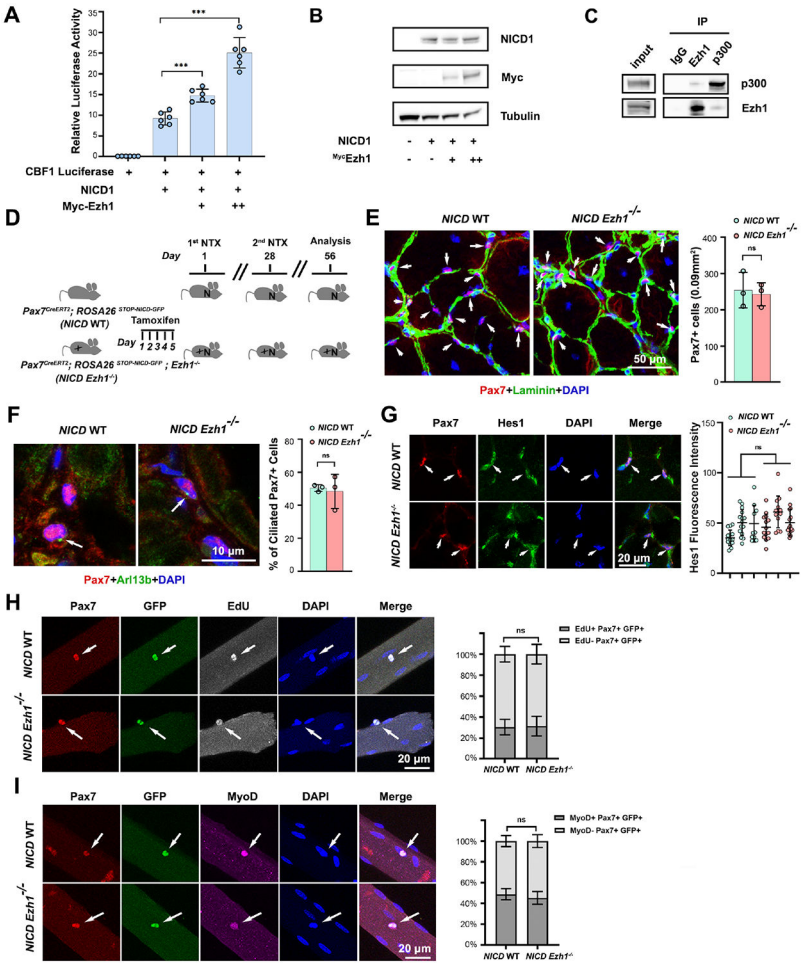

Figure 7. NICD rescues loss of MuSCs and re-establishes MuSCs ciliation in *Ezh1*$^{-/-}$ mice

Relative luciferase activity of C2C12 cells transfected with a Notch reporter construct (multimerized CBF1-luc), a NICD1 expression vector without or with a Myc-tagged Ezh1 (+ 100 ng, ++ 200 ng) expression vector. Data are represented as mean ± SD (n=6), ***p-value <0.001. (B) Immunoblot of transfected C2C12 cells with NICD1, Myc, and Tubulin antibodies. (C) C2C12 cell extracts were immunoprecipitated with IgG, Ezh1, or p300 antibodies and immunoblotted with either Ezh1 or p300 antibodies. (D) Scheme illustrating generation of *Pax7*^{CreERT2}*; ROSA26*$^{STOP\text{-}NICD\text{-}GFP}$ and *Pax7*^{CreERT2}*; ROSA26*$^{STOP\text{-}NICD\text{-}GFP}$*; Ezh1*$^{-/-}$ mice and muscle injury scheme. (E) Laminin and Pax7 immunostaining of TA muscle sections from *Pax7*^{CreERT2}*; ROSA26* $^{STOP\text{-}NICD\text{-}GFP}$ or *Pax7*^{CreERT2}*; ROSA26*$^{STOP\text{-}NICD\text{-}GFP}$*; Ezh1*$^{-/-}$ mice 28 days-2nd injury. Data are represented as mean ± SD (n=3 mice), ns (non significant). (F) Pax7 and Arl13b immunostaining of TA muscle sections from *Pax7*^{CreERT2}*; ROSA26*$^{STOP\text{-}NICD\text{-}GFP}$ or *Pax7*^{CreERT2}*; ROSA26*$^{STOP\text{-}NICD\text{-}GFP}$*; Ezh1*$^{-/-}$ mice 28 days-2nd injury. Data are represented as mean SD (n=3), ns (non significant). (G) Pax7 and Hes1 immunostaining of TA muscle sections from *Pax7*^{CreERT2}*; ROSA26* $^{STOP\text{-}NICD\text{-}GFP}$ or *Pax7*^{CreERT2}*; ROSA26*$^{STOP\text{-}NICD\text{-}GFP}$*; Ezh1*$^{-/-}$ mice 28 days-2nd injury. Hes1 fluorescence intensity data are represented as mean ± SD (n=3 mice), ns (non significant). (H) Pax7, GDP, and EdU immunostaining of myofibers from *Pax7*^{CreERT2}*; ROSA26*$^{STOP\text{-}NICD\text{-}GFP}$ or

Pax7^{CreERT2}*; ROSA26*$^{STOP\text{-}NICD\text{-}GFP}$*; Ezh1*$^{-/-}$ mice. Data are represented as mean ± SD (60 single myofibers from 4 mice). Ns (non significant). (I) Pax7, GFP, and MyoD immunostaining of myofibers from *Pax7*^{CreERT2}*; ROSA26*$^{STOP\text{-}NICD\text{-}GFP}$ or *Pax7*^{CreERT2}*; ROSA26*$^{STOP\text{-}NICD\text{-}GFP}$*; Ezh1*$^{-/-}$ mice. Data are represented as mean ± SD (100 single myofibers from 4 mice), ns (non significant).

KEY RESOURCES TABLE

REAGENT or RESOURCE	SOURCE	IDENTIFIER
Antibodies		
APC anti-mouse CD45	BioLegend	Cat# 103112
Pacific Blue™ anti-mouse Ly-6A/E (Sca 1) Antibody	BioLegend	Cat# 108120
PE/Cyanine7 Streptavidin	BioLegend	Cat# 405206
Biotin anti-mouse CD106 antibody	BioLegend	Cat# 105703
Tri-Methyl-Histone H3 (Lys27) (C36B11) rabbit mAb	Cell Signaling	Cat# 9733
Ezh1 rabbit polyclonal (738)	Mousavi et al.[47]	n/a
Ezh1 (D7D5D) rabbit mAb	Cell Signaling	Cat# 42088S (Lot1)
Ezh1 rabbit polyclonal	Proteintech	Cat# 20852-1-AP
p300 mAb (Clone NM11)	Active Motif	Cat# 61401 (Lot# 31420004)
Rb mAb to Notch1 [EP1238Y]	Abcam	Cat# ab52627 (Lot: GR3236292-25)
Anti-Myc tag, clone9E10	EMD Millipore Corp.	Cat# 05-419 (Lot#3836418)
E7 anti-beta tubulin	Developmental Studies Hybridoma Bank	Cat# E7
Rabbit (DA1E) mAb IgG XP(R) Isotype Control	Cell Signaling	Cat# 3900S (Lot 48)
Mouse (G3A1) IgG1 Isotype Control	Cell Signaling	Cat# 5415S (Lot 13)
Pax7 mouse monoclonal IgG1	Developmental Biology of Hybridoma Bank	Cat# Pax7 supernatant
Pax7 rabbit polyclonal	Thermo Fisher Scientific	PA1-117
MyoD mouse monoclonal IgG1	Santa Cruz Biotechnology	Cat# sc-32758
MyoD rabbit polyclonal	Proteintech	Cat# 18943-1-AP
MyoG mouse monoclonal IgG1	Santa Cruz Biotechnology	Cat# sc-12732
MyoG rabbit monoclonal	Abcam	Cat# ab124800
Laminin rabbit polyclonal	Millipore Sigma	Cat# L9393
Cdkn2a (p16) rabbit polyclonal	Abcam	Cat# ab211542
F4/80 rabbit polyclonal	Thermo Fisher Scientific	Cat# 28463-1-AP
Pdgfra goat polyclonal	R&D Systems	Cat# AF1062
Ezh1	Proteintech	Cat# 20852-1-AP
Hes1 rabbit monoclonal	Thermo Fisher Scientific	Cat# MA5-35063
Arl13b rabbit polyclonal	Proteintech	Cat# 17711-1-AP
a-tubulin mouse monoclonal IgG2b	Millipore Sigma	Cat# T6793
GFP rabbit IgG fraction	Thermo Fisher Scientific	Cat# A111222
Goat anti-Mouse IgG_1 cross-absorbed secondary antibody, Alexa Fluor 488	Thermo Fisher Scientific	Cat# A-21121
Goat anti-Mouse IgG_1 cross-absorbed secondary antibody, Alexa Fluor 555	Thermo Fisher Scientific	Cat# A-21127
Goat anti-Mouse IgG_1 cross-absorbed secondary antibody, Alexa Fluor 647	Thermo Fisher Scientific	Cat# A-21240

REAGENT or RESOURCE	SOURCE	IDENTIFIER
Goat anti-Mouse IgG_{2b} cross-absorbed secondary antibody, Alexa Fluor 555	Thermo Fisher Scientific	Cat# A-21147
Goat anti-Mouse IgG_{2b} cross-absorbed secondary antibody, Alexa Fluor 647	Thermo Fisher Scientific	Cat# A-21242
Goat anti-Rabbit IgG (H+L) Highly Cross-Adsorbed Secondary Antibody, Alexa Fluor Plus 488	Thermo Fisher Scientific	Cat# A32731
Goat anti-Rabbit IgG (H+L) Highly Cross-Adsorbed Secondary Antibody, Alexa Fluor Plus 555	Thermo Fisher Scientific	Cat# A32732
Goat anti-Rabbit IgG (H+L) Highly Cross-Adsorbed Secondary Antibody, Alexa Fluor Plus 647	Thermo Fisher Scientific	Cat# A32733
Bacterial and Virus Strains		
DH5α competent cells	Thermo Fisher Scientific	Cat# 18265017
Chemicals, Peptides, and Recombinant Proteins		
Protein A-Agarose	Roche	Cat# 11134515001
Protein G-Agarose	Roche	Cat# 11719416001
Dynabeads Protein G	Thermo Fisher Scientific	Cat# 10002D
Fibroblast Growth Factor, Basic, Human, Recombinant (rhFGF, Basic)	Promega	Cat# G5071
Dispase, powder	Thermo Fisher Scientific	Cat# 17105041
Collagenase, Type II, powder	Thermo Fisher Scientific	Cat# 17101015
Ham's F-10 Nutrient Mix	Thermo Fisher Scientific	Cat# 11550043
Tamoxifen	Millipore Sigma-Aldrich	Cat# T5648
Notexin	Accurate Chemical&Scientific	Cat# TXL8104-100
Collagenase, Type I, powder	Millipore Sigma-Aldrich	Cat# SCR103
DMEM High Glucose	Thermo Fisher Scientific	Cat# 11995
Critical Commercial Assays		
Picro Sirius Red Stain Kit (Connective Tissue Stain)	Abcam	Cat# ab150681
TRIzol Reagent	Thermo Fisher Scientific	Cat# 15596018
D1000 Screen Tape	Agilent	Cat# 5067-5582
D1000 Reagents	Agilent	Cat# 5067-5583
Chromium Next GEM Chip G Single Cell Kit	10X Genomics	Cat# 1000120
Chromium Next GEM Single Cell 3' Kit v3.1	10X Genomics	Cat# 1000268
Library Construction Kit	10X Genomics	Cat# 1000190
NEBNext Ultra™ II DNA Library Prep Kit for Illumina	NEB	Cat# E7103
NEBNext Ultra™ II RNA Library Prep Kit for Illumina	NEB	Cat# E7775
NEBNext Poly(A) mRNA Magnetic Isolation Module	NEB	Cat# E7490
Quant-iT™ PicoGreen™ dsDNA Assay Kits and dsDNA Reagents	Thermo Fisher Scientific	Cat# P7589
Click-iT Plus TUNEL Assay Alexa Fluor 594	Thermo Fisher Scientific	Cat# C10618
Illumina Tagment DNA TDE1 Enzyme and Buffer Kits	Illumina	Cat# FC-121-1030
High-Capacity cDNA Reverse Transcription Kit	Thermo Fisher Scientific	Cat# 4368813
SYBR green PCR master mix	Thermo Fisher Scientific	Cat# 4312704

REAGENT or RESOURCE	SOURCE	IDENTIFIER
Lipofectamine 3000 transfection reagent	Thermo Fisher Scientific	Cat# L3000001
Dual-luciferase reporter assay system	Promega	Cat# E1910
Insulin-Transferrin-Selenium (ITS-G) (100X)	Thermo Fisher Scientific	Cat# 41400045
NuPAGE™ 4 to 12%, Bis-Tris, 1.0–1.5 mm, Mini Protein Gels	Thermo Fisher Scientific	Cat# NP0322BOX
NuPAGE™ LDS Sample Buffer (4X)	Thermo Fisher Scientific	Cat# NP0007
NuPAGE™ Sample Reducing Agent (10X)	Thermo Fisher Scientific	Cat# NP0009
Nitrocellulose/Filter Paper Sandwich, 0.45 μm, 8.3 x 7.3 cm	Thermo Fisher Scientific	Cat# LC2001
Click-iT™ TUNEL Alexa Fluor Imaging Assays for Microscopy & HCS	Thermo Fisher Scientific	Cat# C10245
Click-iT™ EdU Cell Proliferation Kit for Imaging, Alexa Fluor™ 555 dye	Thermo Fisher Scientific	Cat# C10338
RNeasy Mini Kit (50)	Qiagen	Cat# 74104
Deposited Data		
RNAseq, ChIPseq, ATACSeq, scRNAseq data	This paper	GSE219232
RNA-seq data from freshly FACS-isolated and 48 hr-activated MuSCs	Ryall et al.[54]	GSE64379
scRNAseq data from FACS-isolated MuSCs and primary myoblasts	Dell'Orso et al.[55]	GSE126834
Experimental Models: Cell Lines		
C2C12 cell line	ATCC	Cat# CRL-1772
Primary Myoblasts	This study	N/A
Experimental Models: Organisms/Strains		
C57BL/6J mice	The Jackson Laboratory	Cat# 000664
Tamoxifen inducible *Pax7*^{CreERT2} mice	The Jackson Laboratory	Cat# 017763
Nuclear membrane binding *ROSA26*$^{STOP\text{-}Sun\text{-}1\text{-}GFP}$ mice	The Jackson Laboratory	Cat# 021039
ROSA26$^{STOP\text{-}NICD\text{-}GFP}$ mice	The Jackson Laboratory	Cat# 008159
Ezh1-null mice (*Ezh1*$^{-/-}$)	Dr. Lothar Hennighausen (NIDDK, NIH)	Research Institute of Molecular Pathology, Ezhkova et. al. [29]
Pax7^{CreERT2} ; *ROSA26*$^{STOP\text{-}Sun\text{-}1\text{-}GFP}$ mice	This study	N/A
Pax7^{CreERT2} ; *ROSA26*$^{STOP\text{-}Sun\text{-}1\text{-}GFP}$; *Ezh1*$^{-/-}$ mice	This study	N/A
Pax7^{CreERT2}; *ROSA26*$^{STOP\text{-}NICD\text{-}GFP}$	This study	N/A
Pax7^{CreERT2}; *ROSA26*$^{STOP\text{-}NICD\text{-}GFP}$; *Ezh1*$^{-/-}$	This study	N/A
NOD-*Rag1*^{null} *IL2rg*^{null}	The Jackson Laboratory	Cat# 007799
Oligonucleotides		
q-RT-PCR Primer Sequences	Thermo Fisher Scientific	Supplemental Table S4
Recombinant DNA		
8xCBF1-luc (pJH26)	Dr. Diane Hayward	Johns Hopkins University
pCAGGS-NICD	Addgene	Cat# 26891
pHAN-Myc-Ezh1	Mousavi et al.[47]	N/A
pHAN-Myc-Ezh1ΔSET	Mousavi et al.[47]	N/A

REAGENT or RESOURCE	SOURCE	IDENTIFIER
pRL	Promega	Cat# E2241
Software and Algorithms		
Image J FUJI	Open platform	https://fiji.sc/
Biorender	Web based	https://www.biorender.com/
Image-Pro 9.2	Media Cybernetics	http://microopticalsolutions.com/media-cybernetics
ZEN 3.5 Blue Edition	Carl Zeiss	https://www.zeiss.com/microscopy/en/products/software/zeiss-zen.html
Adobe Photoshop 2022	Adobe	https://www.adobe.com/products/photoshop.html
GraphPad Prism 9	GraphPad	https://www.graphpad.com/scientific-software/prism/
Trimgalore ver. 0.6.6	N/A	https://www.bioinformatics.babraham.ac.uk/projects/trim_galore/
TopHat ver.2.1.1	Trapnell et al.[127]	https://ccb.jhu.edu/software/tophat/index.shtml
MACS ver.1.4.2	Zhang et al.[134]	https://pypi.org/project/MACS/1.4.2/
Bowtie ver. 1.1.1	Langmead et al.[133]	https://bowtie-bio.sourceforge.net/index.shtml
CellRanger ver. 3.0.2	10x Genomics	https://support.10xgenomics.com/single-cell-gene-expression/software/release-notes/3-0
Seurat v4.1.0	Stuart et al.[129]	https://cran.r-project.org/web/packages/Seurat/index.html
Monocle2	Trapnell et al.[131]	http://cole-trapnell-lab.github.io/monocle-release/docs/
Monocle3	Cao et al.[132]	https://cole-trapnell-lab.github.io/monocle3/
Custom scripts	This paper	https://doi.org/10.5281/zenodo.7790116
Other		
5 mL Polypropylene Round-Bottom Tube	Falcon	Cat# 352063
5 mL Polystyrene Round-Bottom Tube with Cell-Strainer Cap	Falcon	Cat# 352235
20 G BD™ Needle 1 in. single use, sterile	BD Biosciences	Cat# 305175
BD Luer-Lok tip control syringe, 10-ml	BD Biosciences	Cat# 309604
Falcon® 40 μm Cell Strainer, Blue, Sterile	Corning	Cat# 352340
Falcon® 60 mm TC-treated Cell Culture Dish, Sterile	Corning	Cat# 353002
Falcon® Centrifuge Tubes, Polypropylene, Sterile, Corning®, 15-ml	VWR	Cat# 352196
Falcon® Centrifuge Tubes, Polypropylene, Sterile, Corning®, 50-ml	Corning	Cat# 352070
Falcon® Round-Bottom Tubes, Polypropylene, Corning®	VWR	Cat# 60819-728
Falcon® Round-Bottom Tubes, Polystyrene, with 35um Cell Strainer Cap Corning®	VWR	Cat# 21008-948

REAGENT or RESOURCE	SOURCE	IDENTIFIER
Hardened Fine Scissors	Fine Science Tools Inc	Cat# 14090-09
Student Dumont #5 ForcepsFine Science Tools Inc91150-20	Fine Science Tools Inc	Cat# 91150-20
Student Vannas Spring Scissors	Fine Science Tools Inc	Cat# 91500-09